Spring 5-12-2018

A FACILE METHOD TO SYNTHESIZE BI-FUNCTIONAL NANOSTRUCTURED NICKEL COMPOUNDS FOR ENERGY STORAGE AND WATER SPLITTING APPLICATIONS

Nawaf Albeladi
Pittsburg State University, nalbeladi@gus.pittstate.edu

A FACILE METHOD TO SYNTHESIZE BI-FUNCTIONAL NANOSTRUCTURED NICKEL COMPOUNDS FOR ENERGY STORAGE AND WATER SPLITTING APPLICATIONS

A Thesis Submitted to the Graduate School
in Partial Fulfillment of the Requirements
for the Degree of the
Master of Science

Nawaf Albeladi

Pittsburg State University

Pittstburg, Kansas

May, 2018

A FACILE METHOD TO SYNTHESIZE BI-FUNCTIONAL NANOSTRUCTURED NICKEL COMPOUNDS FOR ENERGY STORAGE AND WATER SPLITTING APPLICATIONS

Nawaf Albeladi

APPROVED:

Thesis Advisor _____
Dr. Ram Gupta, Department of Chemistry

Committee Member_____
Dr. Khamis Siam, Department of Chemistry

Committee member_____
Dr. Pawan Kahol, Department of Physics

Committee Member_____
Dr. John Franklin, Department of English and Modern Languages

ACKNOWLEDGEMENTS

First, I must express my very profound gratitude to my parents and to my wife and daughter for providing me with unfailing support and continuous encouragement throughout my years of study and through the process of researching and writing this thesis. This accomplishment would not have been possible without them.

I would like to sincerely thank my thesis advisor Dr. Ram Gupta. The door to Prof. Gupta's office was always open whenever I had a question about my project. He consistently allowed this paper to be my own work but steered me in the right direction whenever he thought I needed it.

In addition, I would like to express the deepest appreciation to all my committee members, Dr. Khamis Siam, Dr. Pawan Kahol, and Dr. John Franklin, as well as other faculty members in the Chemistry Department at Pittsburg State University.

I also would like to thank Dr. Sanjay Mishra, at the University of Memphis, who was involved in the thesis for recording the SEM images.

Finally, I would like to thank all my friends for their support and encouragement during my journey towards this degree.

A FACILE METHOD TO SYNTHESIZE BI-FUNCTIONAL NANOSTRUCTURED NICKEL COMPOUNDS FOR ENERGY STORAGE AND WATER SPLITTING APPLICATIONS

An Abstract of the Thesis by
Nawaf Albeladi

In recent years, the increasing demands for clean, efficient, and renewable energy have triggered researchers to increase their effort to develop multi-functional materials for energy applications. Supercapacitors, among the comparative energy storage devices, have attracted considerable attention due to their high energy storage capacity, fast charge-discharge capability, long cycle life, and high power density. Transition metal oxides and sulfides are being used as materials for supercapacitor applications due to their excellent conductivity, high electrochemical properties, and large theoretical energy storage capacitance. On the other hand, among the numerous energy techniques, water splitting has become one of the most important technologies recently due to its ability to produce hydrogen and oxygen as renewable and clean fuels in a sustainable way. Transition metal oxides are one of the most promising alternative candidates for noble metal due to its interesting properties in water splitting fields. In this regard, we have used a facile hydrothermal method to synthesize nanostructured nickel hydroxide, nickel oxide, and nickel sulfide in presence of cetyltrimethylammonium bromide (CTAB) and polyvinylpyrrolidone (PVP) on nickel foams using a binder-free approach. These synthesized nanostructured materials are used for both supercapacitor applications and as catalysts for water splitting. The structures, morphologies, and electrochemical performances of the synthesized nickel compounds (nickel hydroxide, nickel oxide, and nickel sulfide) were analyzed and characterized using a variety of techniques. For the

structural characterizations, the X-ray diffraction, and scanning electron microscopy, were used. The XRD patterns confirmed the phase purity of all the synthesized samples. The average crystallite size of all the samples was also estimated using the Scherrer equation based on the most intense peak. The morphological structure and the size of the samples were analyzed via SEM, and they were observed to depend on the growth condition and presence of CTAB and PVP.

The electrochemical performances of the samples toward supercapacitors and catalysts applications were performed in a standard three-electrode system using potassium hydroxide as an electrolyte, a Pt wire as a counter electrode, a saturated calomel electrode as a reference electrode, and the synthesized electrodes as a working electrode. The potential applications for supercapacitors and catalysts were investigated via cyclic voltammetry, galvanostatic charge-discharge measurements, electrochemical impedance spectroscopy, and linear sweep voltammetry. The electrochemical performance of the synthesized nanostructured materials revealed that their properties depend on the presence of CTAB and PVP during synthesis. The areal capacitance was observed to be 67, 859, and 2,633 mF/cm^2 for NiO, $Ni(OH)_2$, and NiS_2, respectively. On the other hand, the electrocatalytic performances toward oxygen evolution reaction (OER) and hydrogen evolution reaction (HER) were investigated. The NiS_2-CTAB electrode showed the lowest OER overpotential of 298 mV at 10 mA/cm^2 and relatively a low Tafel slope of 111 mV/dec. The lowest HER overpotential of 177 mV at 10 mA/cm^2 was observed for the $Ni(OH)_2$-PVP electrode. Our results suggest that nickel-based nanostructured materials could be used as bi-functional materials for energy storage and generation applications.

TABLE OF CONTENTS

LIST OF TABLES

LIST OF FIGURES

CHAPTER I

INTRODUCTION

1.1 Energy Issues that have been the Most Concern

In the past decades, energy has become one of the most significant issues facing humanity. The tremendous growth of the worldwide economy, a notable increase in environmental pollution, a constant diminution of fossil fuels, and the energy crisis in between consumption and wasting, have increased and promoted the demands of clean, sustainable and efficient energy resources.

Currently, it is estimated that we use over a million terajoules of energy every day. The growth of the global population, as well as the industrialization of developing countries, are some of the main reasons why there is such a high global energy consumption. Besides the heavy consumption, another issue in energy is that about half of the energy consumed is fossil fuel, which is known to have adverse effects on the environment including global warming and acidic rain.

Another issue brought about by the use of fossil fuel is that it is a non-renewable type of energy. This means that it has a limited supply. It is estimated that about one hundred and thirty-five billion tons of oil have been used in powering vehicles already [1]. The rise in energy demand globally has led to the hike in prices for energy. Experts predict that in the future, prices are expected to rise more drastically. Given the role that energy

plays in our daily lives, the scarcity is predicted to have potentially devastating effects on our lives and of civilization as we know it. All these issues discussed already would suggest that the best thing to do would be to quickly shift to better sources of energy, such as non-renewable energy.

1.2 Types of Energy

Energy is mainly categorized according to its renewability. There are two kinds of energy; these are renewable and non-renewable. Due to the long time it takes to replenish, non-renewable energy is in limited supply.

Non-renewable energy includes nuclear energy, coal, natural gas, and oil.

i. Nuclear energy is created by the fission of nuclear fuel. Although it may not pollute the air since it is carbon-free, it has numerous limitations which include expense, and security issues associated with it.

ii. Coal is a sedimentary rock which among other things is made of combustible matter. It was the main source of energy in the Industrial Revolution. However, it contains impurities such as nitrogen and sulfur which causes negative effects on the environment.

iii. Oil is a naturally occurring combustible liquid. It supplies around 40% of the total energy consumed and about 99% of it is used in transportation.

Renewable energy, on the other hand, is replenished in a short period of time. Major sources of renewable energy include solar energy, wind energy, hydro energy, and energy via water splitting. These environmental-friendly types of energy are commonly referred to as green energy.

1.2.1 Solar Energy

Due to the improving technology in solar energy, people are switching to solar energy. Photovoltaic cells change light into electricity [2,3]. Although it is considered as the most efficient way to get electricity produced, its main limitation is the amount of sun that reaches the surface of the earth [4], which is dependent on time, geographical area, and weather, as well as season.

1.2.2 Wind Energy

It is considered as the fastest growing renewable source of energy due to its availability and renewability. Wind energy converts the kinetic energy of wind to energy that can be used as electric and mechanical energy [5]. It uses turbines which are categorized into horizontal, and vertical axis depending on their rotor axis. The main limitation in using this energy is that it is dependent whether the wind is blowing or not. This is usually affected by the weather, which can be unpredictable. This limitation justifies the need for energy storage systems.

1.2.3 Hydro Energy

Due to its efficiency in electricity production, hydro energy is considered as one of the most efficient ways to produce electricity. It is the most used renewable energy. Energy is produced by the motion of water which turns turbines to produce electric and mechanical energy [2]. The amount of energy depends on the volume of water, and the speed of flow. The main limitation of hydro energy is the availability of water. During droughts, for example, the amount of electricity produced becomes limited. Another drawback of hydropower is the negative effect on water wildlife.

Energy sources are also classified as either primary or secondary. In the primary sources, energy is extracted directly from the environment. Renewable and non-renewable energy are classified as primary sources of energy. On the other hand, secondary energy is converted from primary energy and is in the form of electricity.

1.2.4 Energy via Water Splitting

Water molecules can be split into hydrogen and oxygen, through the addition of energy to an H_2O molecule that can transform it to H_2 and O_2. Among the numerous energy techniques, water splitting has become one of the most important technologies due to its ability to produce hydrogen and oxygen as renewable and clean fuels in a sustainable way. Hydrogen evolution reaction (HER) and oxygen evolution reaction (OER) are obtained through water electrolysis. Due to the slow kinetic and the involvement of several steps, the OER requires a higher overpotential than the HER [6]. Recently, transition metal oxides have been considered as one of the most promising alternative candidates for noble metal due to their interesting properties in water splitting fields [7].

1.3 The Need to Store Energy

It is estimated that the demand for energy is going to double midway through this century, and will triple before it ends [1]. Therefore, it is safe to say that there is the need for energy storage because with the increasing demand there might come a time that the energy generated will not meet demand. The increase in energy demand can be attributed to the changes in the living standards of people. It is also a fact that because some energy sources are harmful to the environment, many countries have decided to turn to renewable sources to generate energy.

Most of these renewable energy sources are dependent on climate or, rather,

weather conditions. For instance, wind and solar energies cannot be generated if the wind is not blowing or if the sun is not shining. As a result of this, it is important to store energy for future uses in case the favorable conditions for energy generation are not present. Moreover, consumers should not be left to suffer just because certain favorable conditions for generating energy are lacking, thus the need for creating storing energy.

Storing energy is not only important because it smooths the fluctuations that arise from changes in weather (thus increasing reliability) but also increases resilience in small and large substations. Although some energy storing devices are expensive and have both advantages and disadvantages, it still is important to store energy.

In response to the significant demands for improving and developing more efficient energy technology that can store the created energy and release it when needed, there has been great interest in this field. Knowing the mechanisms of the energy storage technologies give a better understanding to develop and refine efficient energy storage devices. The energy storage technologies can be divided into many types based on mechanisms such as chemical, electrochemical, thermal, and physical processes. Fuel cells, batteries, capacitors, and supercapacitors are currently the most well-known devices for storing energy. **Figure 1.1** shows a comparison plot of specific power *vs.* specific energy for various electrical energy storage devices [8]. The data illustrate that the energy stored by supercapacitors is higher than that stored by conventional capacitors, and that supercapacitors are able to deliver more power than batteries.

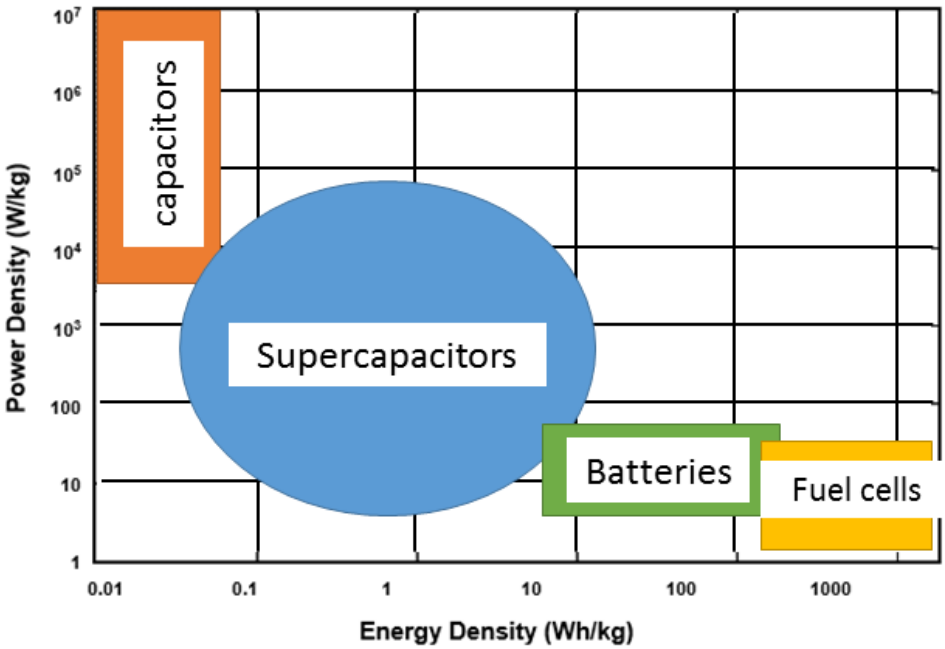

Figure 1.1: Specific power *vs.* specific energy for various electrical energy storage devices.

1.4 Energy Storage Devices

1.4.1 Fuel Cells

A fuel cell makes use of chemical energy to generate power just as it is the case with batteries. It can be defined as an electrochemical device in which a reaction between a fuel such as methanol or hydrogen and an oxidant such as air or oxygen converts the fuel's chemical energy into electrical energy directly without combustion [9]. The difference between a fuel cell and a battery is that a fuel cell is like a chemical battery and that its reactants are not a part of the battery but come from external sources. The reactants have to be refilled from time to time, unlike a battery which stores electrical energy chemically in a closed system.

Normally, a fuel cell needs a lot of minor equipment such as cooling systems, fuel pumps, recirculators, and fuel tanks [10]. Due to this, it is almost impossible to use them in applications that are portable. However, the invention of some devices such as the small direct methanol fuel cell (DMFC), which does not need most of the extraneous equipment, makes it easier to use them [10]. The size of fuel cells varies from hand-held systems megawatt power stations. Despite the fact that proton-exchange fuel cells (PEMFC) can operate at room temperature, most of the large ones operate at 200 to 1000 degrees Celsius.

Fuel cells are most efficient at high temperatures and over a narrow range of performance parameters, and when power demands are high they rapidly become inefficient. Also, they are expensive because they use catalyst metals such as platinum. Most of the times they are used together with either supercapacitors or batteries in order to provide a high power, high energy combination [10].

1.4.2 Batteries

The invention and credit of the term “batteries” goes to Benjamin Franklin in 1748 when he wanted to describe an array of charged glass plates he made [11]. A battery is a multi-celled direct current voltage device that generates electrical energy through the conversion of either solar, thermal, nuclear or chemical energy. Batteries are self-contained as they store either of the aforementioned energies in order to convert them on demand. Primary and secondary batteries are the two broad categories of batteries. Anode, cathode, and electrolyte are three basic components of all batteries, whether primary or secondary and they can be used to determine the performance and properties of a battery.

Primary batteries, which are also known as traditional batteries, are the most widely used. They are designed as single-use batteries because after use they are either disposed

or recycled; they cannot be recharged. However, they have a high impedance which means that at low current loads they have a long life. Zinc-air, carbon-zinc, alkaline, lithium metals, and silver oxide are the most commonly used primary batteries. In general, primary batteries are less effective because of their limited capacities of used materials.

Secondary or rechargeable batteries can be recharged up to even a thousand times depending on the usage and battery type; but their capability to store energy is lower than that of primary ones. They rely on an electric current to reverse the chemical reactions that take place during a discharge. Short shallow discharges usually result in long cycle life whereas deep discharges result in short cycle life. The charge time dependent on the depth of discharge and battery condition among other factors, ranges from 1 to 12 hours. Commonly used secondary batteries are nickel-cadmium, lithium-ion, lead acid, lithium metal, and nickel-metal hydride [12]. Despite their limited power and life, disposal concerns, and limited power, rechargeable batteries have a wide range of applications.

1.4.3 Capacitors

A capacitor is another energy storage device that makes use of a physical charge between its two electrodes to store energy as shown in **Figure 1.2**. Capacitors normally have two plates separated by insulators that conduct electricity; the insulator is called a dielectric layer. Positive charges are led to one plate while the negative is led to the other one by the potential difference (V) between the two plates. Capacitors store energy on the surfaces of metal electrodes or metalized plastic film. A capacitor's storage charge is equal to V which is the potential difference between the two plates, thus the equation;

$$C = \frac{Q}{V} \quad \text{……. (1)}$$

Where C is the capacitance, Q is the charge on both plates, and V is the potential

applied.

While capacitors deliver high currents, they do so for short periods of time because they have relatively low capacitance. It is because of this reason that their applications to consumer electronics are limited [13].

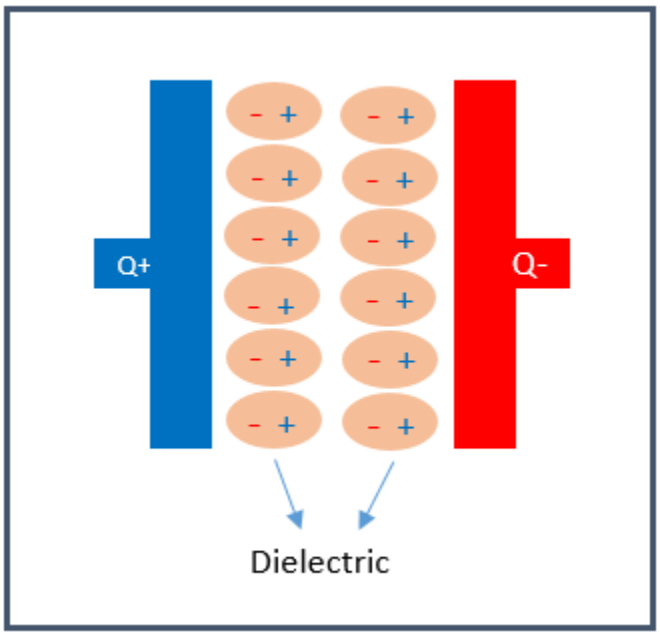

Figure 1.2: Capacitor aligns molecules of dielectric across an electric field to store energy.

1.4.4 Supercapacitors

Supercapacitors, which are also known as ultracapacitors and electrochemical capacitors, are one of the most promising energy storage devices. Supercapacitors have been widely investigated for various applications such as portable devices and electric vehicles due to their high energy storage capacity, fast charge-discharge capability, long

cycle life, and high power density [14,15]. A normal capacitor can be improved to become a supercapacitor by utilizing porous carbon or nanostructured metal oxide [15]. One difference between a capacitor and a supercapacitor is that the supercapacitors use a molecule-thin layer of electrolyte while the capacitor uses a dielectric to separate charge [6]. Another difference is that supercapacitors offer very high capacitance but in small packages. Generally, capacitors can be divided into three types based on the charge-storage mechanism, electrical double-layer capacitors (EDLC), electrochemical pseudocapacitors, and hybrid capacitors [16] as seen in **Figure 1.3**.

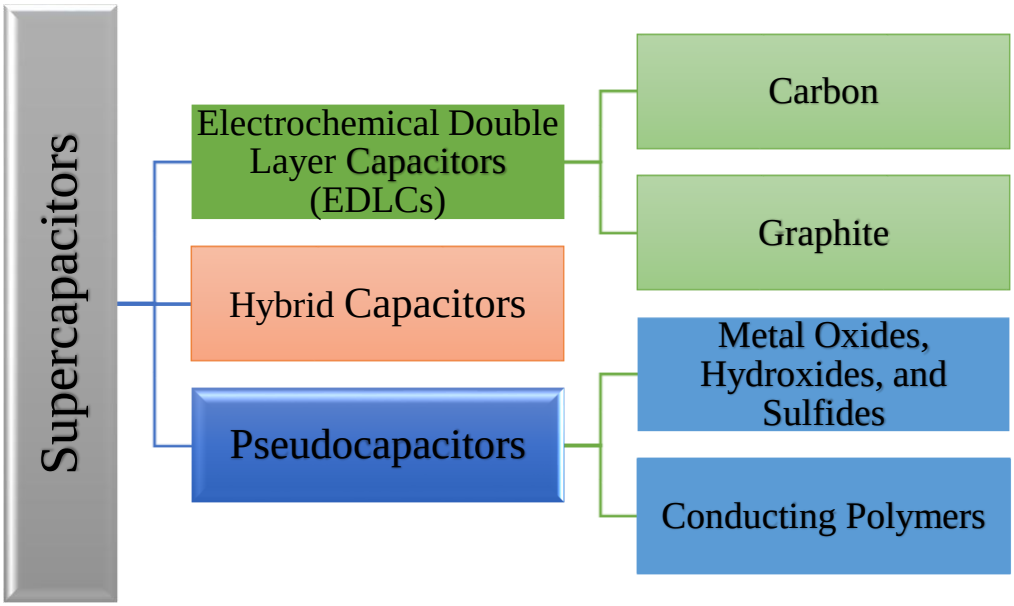

Figure 1.3: The types of supercapacitors.

1.4.4.1 Electrical Double-Layer Capacitors

This is the most common and least costly of the manufactured type of supercapacitors. ELDCs store the charge electrostatically using the very thin double-layer structure formed at the interface between electrode and electrolyte; thus, there is no transforming of charge between the electrode and electrolyte (a non-faradaic reaction),

[16]. The electrolyte ion is led to move to the small voids that produce different polarity at the electrodes by the potential difference of the ELDCs. Nonetheless, the rods are designed so that they prevent the ions from combining again and that is the reason why a double layer of charge is produced on both electrodes [17]. The double layers decrease the distance between the electrodes and increase the surface area; in this way, ELDCs are able to attain greater densities than conventional capacitors [18]. The carbon electrode-based materials such as active carbon, carbon nanotubes, and graphene are common electrode materials for the EDLCs.

1.4.4.2 Pseudocapacitors

In contrast, with pseudocapacitors the charge is stored electrochemically and is dominated by a faradic reaction via a fast and reversible reduction-oxidation reaction at the electrode/electrolyte interface [21]. An electrochemical active material can be added to carbon electrode materials to increase the capacitance in this type of capacitors making them better than ELDCs [16]. Transition metal oxides, hydroxides, sulfides, and conducting polymers are the most common electrode materials for pseudocapacitors due to their high electrochemical activity. Among them, manganese oxide (MnO_2), ruthenium oxide (RuO_2), cobalt sulfide (Co_9S_8), and cobalt oxide (Co_3O_4) are particularly attractive [19,20]. Pseudocapacitors exhibit higher capacitance and higher energy density in comparison with ELDCs [24].

1.4.4.3 Hybrid Capacitors

As the name suggests, hybrid capacitors incorporate both faradaic and non-faradaic processes to store a charge; they have the properties of both ELDCs and pseudocapacitors [16]. As a result of this combination, hybrid capacitors have greater power density, cycling

stability, and energy than the other two types of capacitors [13]. Because of this, hybrid capacitors can be used for various applications with lower costs, such as transport and wind power generation systems.

To conclude on supercapacitors, they are advantageous for the reason that they possess high power density; and, because of their ability to charge and discharge in a simple way and faster than batteries [13]. Their high cycle life and controllable charge are also better than batteries.

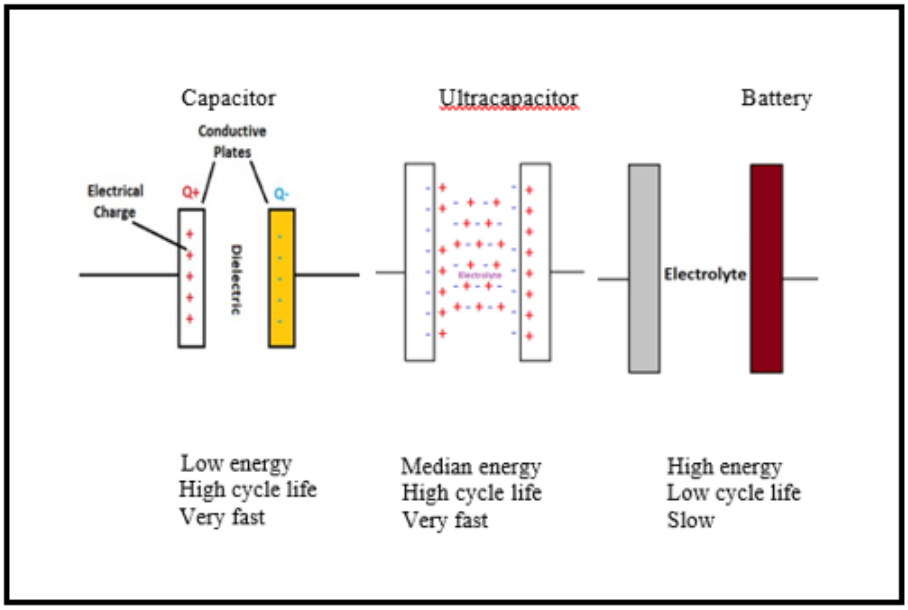

Figure 1.4: Comparison among capacitors, ultracapacitors, and batteries.

1.5 Electrochemical Water Splitting Applications

As a result of the increase in the demand for energy and the continuous depletion of energy sources, water splitting is attracting considerable research attention to replace the traditional fossil fuels in a sustainable way with zero carbon emission. Also, there has been

an increase in the concerns for global warming, thus creating the need for clean energy production technologies [21]. Water splitting is referred to as the chemical reaction where water is separated into its molecular compounds, which are hydrogen and oxygen [10]. These gases are separated from each other under a potential often higher than the theoretical one of water electrolysis in order to obtain them in their pure state as much as possible [5]. Oxygen evolution reaction catalysts work best in an alkaline environment while hydrogen evolution reaction catalysts perform best in acidic conditions.

The water splitting reaction: $2H_2O_{(l)} \longrightarrow 2H_{2(g)} + O_{2(g)}$

Hydrogen evolution reaction: $2H^+_{(eq)} + 2e^- \longrightarrow H_{2(g)}$

Oxygen evolution reaction: $4OH^-_{(eq)} \longrightarrow 2H_2O_{(l)} + O_{2(g)} + 4e^-$

Recently, transition metal oxides, hydroxides, phosphides, and sulfides such as Cu_2S, MoS_2, CoP are being used as alternative catalysts for noble metals. In this project, we developed efficient, stable, and inexpensive bi-functional electrocatalysts for the oxygen evolution reaction and hydrogen evolution reaction. **Figure 1.5** represents water splitting for the oxygen evolution reaction and the hydrogen evolution reaction.

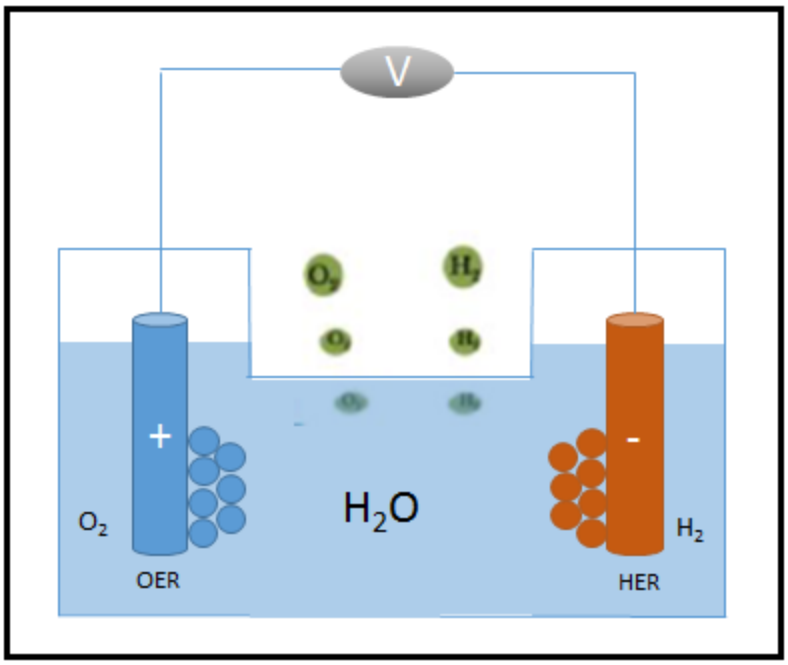

Figure 1.5: Schematic represents water splitting with the oxygen and the hydrogen evolution reaction being produced.

1.6 Project Rationale

The primary objective of this thesis is to use a facial hydrothermal technique to synthesize bi-functional nanostructured nickel compounds in the presence of cetyltrimethylammonium bromide and polyvinylpyrrolidone on nickel foams using a binder-free approach then to study their characteristics using X-ray diffraction and scanning electron microscopy. In addition, another objective is to investigate their potential applications toward energy storage for supercapacitors and catalysts for oxygen evolution reaction and hydrogen evolution reaction using different techniques such as cyclic voltammetry, galvanostatic charge-discharge measurements, electrochemical impedance spectroscopy, and linear sweep voltammetry.

CHAPTER II

EXPERIMENTAL CHARACTERIZATIONS

2.1 Materials Used

The following reagents of analytical grade were used and employed without any further purification: nickel (II) nitrate hexahydrate $Ni(NO_3)_2.6H_2O$ (Sigma-Aldrich), sodium sulfide Na_2S (Acros-Organics), urea $CO(NH_2)_2$ (Fisher Sci), ethanol C_2H_5OH, deionized (DI) water, polyvinylpyrrolidone (PVP) (Acros-Organics), cetyltrimethylammonium bromide (CTAB) (Acros-Organics), and nickel (Ni) foam.

2.2 Synthesis of Nickel Hydroxide ($Ni(OH)_2$), Nickel Oxides (NiO), and Nickel Sulfides (NiS_2)

All the samples were synthesized using a hydrothermal method. Before the hydrothermal treatment, in a 3M HCl solution, Ni foam was immersed and sonicated for ten minutes in order to remove the surface oxide layer. After that, the Ni foam was sequentially washed and cleaned with DI water and ethanol, respectively. Then, the Ni foam was dried in a vacuum oven overnight.

2.2.1 Preparation of Nanostructured $Ni(OH)_2$-CTAB & $Ni(OH)_2$-PVP

In a typical synthesis, 0.997×10^{-3} mole of $Ni(NO_3)_2.6H_2O$ was dissolved in 5 ml DI water. Then, 9.99×10^{-3} mole of urea was added to this solution and stirred for five

minutes using magnetic stirring. In another beaker, 3.03×10^{-3} mole of CTAB was dissolved in 10 ml DI water. The CTAB solution was added to the first solution and stirred for an additional five minutes using magnetic stirring. After that, 15 ml of ethanol was added to the above solution and sonicated for ten minutes. The mixture was transferred into a 45 mL Teflon-lined stainless-steel autoclave containing a piece of nickel foam at the bottom, which was then heated at 120 ℃ for a period of 12 hours in an electric oven then allowed to cool down to room temperature. The Ni foam was taken out, and the precipitate was collected. Both (the Ni foam and precipitate) were washed with DI water and ethanol several times then dried in a vacuum oven at 60 ℃ overnight. Likewise, the $Ni(OH)_2$-PVP sample was prepared, but the 2.66×10^{-3} mole of PVP was used instead of CTAB.

2.2.2 Preparation of Nanostructured NiO-CTAB & NiO-PVP

The NiO-CTAB & NiO-PVP were synthesized through a calcination method using the intermediate $Ni(OH)_2$-CTAB & $Ni(OH)_2$-PVP. For this, the as-synthesized intermediate products (Ni foam and powder) were calcined at 350 ℃ (5℃ /min) in the air for two hours to completely convert the precursor to a nickel oxide phase. The color of the samples was observed to change to brown after calcination. Likewise, the NiO-PVP was prepared.

2.2.3 Preparation of Nanostructured NiS_2-CTAB & NiS_2-PVP

NiS_2-CTAB & NiS_2-PVP were prepared by sulfurizing $Ni(OH)_2$-CTAB & $Ni(OH)_2$-PVP, respectively, using a hydrothermal method. For this, $Ni(OH)_2$ samples were immersed in 30 mL of 0.2M Na_2S solution in a 45 ml Teflon-lined autoclave separately, and then it was sealed and maintained at 140 ℃ for twenty-four hours. Finally, the obtained NiS_2 samples grown on Ni foam and the precipitate were washed with ethanol and DI water

several times respectively. The samples and the powder were dried in a vacuum oven at 60 °C overnight.

2.3 Characterizations

The structures, morphologies, and electrochemical performance of the synthesized nickel compounds (nickel hydroxide, nickel oxide, and nickel sulfide) were analyzed and characterized using a variety of techniques. For the structural characterizations, X-ray diffraction (XRD) and scanning electron microscopy (SEM) were used. For electrochemical investigations, cyclic voltammetry (CV), galvanostatic charge-discharge measurements (GDC), electrochemical impedance spectroscopy (EIS), and linear sweep voltammetry (LSV) were used. More details of these characterization techniques are given below.

2.3.1 X-Ray Diffraction

The X-ray diffraction contains three fundamental elements: an X-ray tube, a sample holder, and an X-ray detector. The principle of X-ray diffraction relies on exciting the electrons by heating a filament in an X-ray electrode tube to create an X-ray. When the exciting electrons return to the most stable level, they release energy as X-ray photons. X-ray diffraction using a Shimadzu X-ray diffractometer set on the 2θ-θ scan with $CuK_{\alpha 1}$ (λ=1.5406 Å) radiation was performed in order to analyze the structure, phase purity, and crystallographic data of these synthesized materials. The X-ray was generated at a voltage of 40 KV with a 30 mA current. The diffraction patterns of the sample were recorded over the scanning angle range of 10° to 80°. The X-ray detector was set at a point that could achieve symmetrical status so that the angle between the atomic planes and the detector would be 2 θ, as shown in **Figure 2.1.**

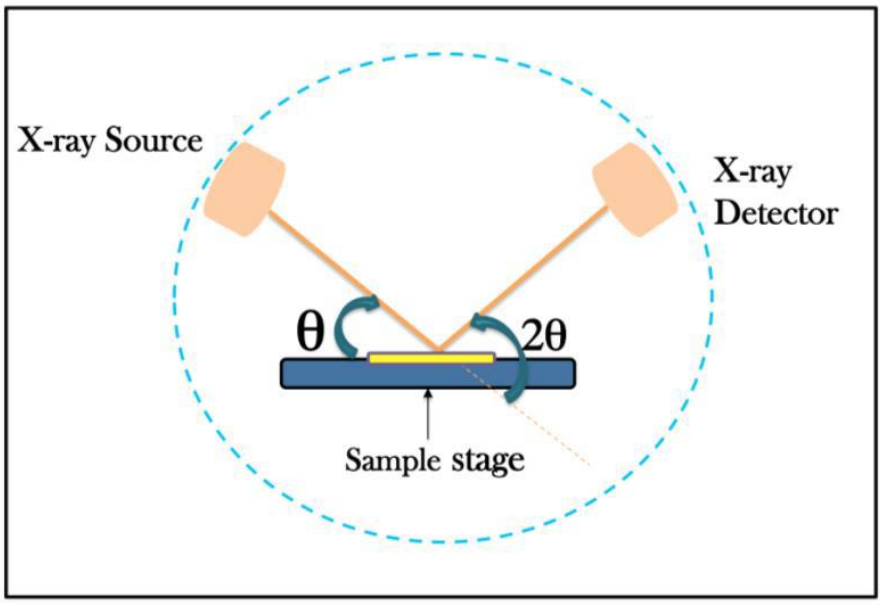

Figure 2.1: Schematic diagram of X-ray diffractometer.

2.3.2 Scanning Electron Microscopy

The detailed morphology and structure characteristics of the synthesized samples were investigated via SEM characterization. The value of the scanning electron microscope instrument is reflected in its ability to produce a picture of a sample when scanned via concentrated radiation of electrons at its surface. Also, the scanning electron microscope permits an observation and characterization of a material on a range of micrometer (μm) to nanometer (nm). The particle size and morphological structure of all the synthesized samples were investigated via a JEOL JSM-840A scanning electron microscope at the University of Memphis.

2.3.3 Electrochemical Characterization

The main objective of these experiments is to electrochemically study the performances and properties of all six samples, $Ni(OH)_2$-CTAB, $Ni(OH)_2$-PVP, NiO-CTAB, NiO-PVP, NiS_2-CTAB, and NiS_2-PVP for supercapacitor and catalyst applications. All the electrochemical measurements were performed at room temperature using a three-electrode system. The typical three-electrode cell system contains a reference electrode (a saturated calomel electrode), a counter electrode (a platinum wire), and a working electrode (synthesized nanostructured metal hydroxide, oxide, and sulfide grown on nickel foam). All the electrochemical tests were conducted with a VersaStat 4-500 electrochemical workstation (Princeton Applied Research, USA). VersaStudio software provided by Princeton Applied Research was employed for the analysis of the electrochemical data. **Figure 2.2** depicts the design of a three-cell electrochemical measurement system.

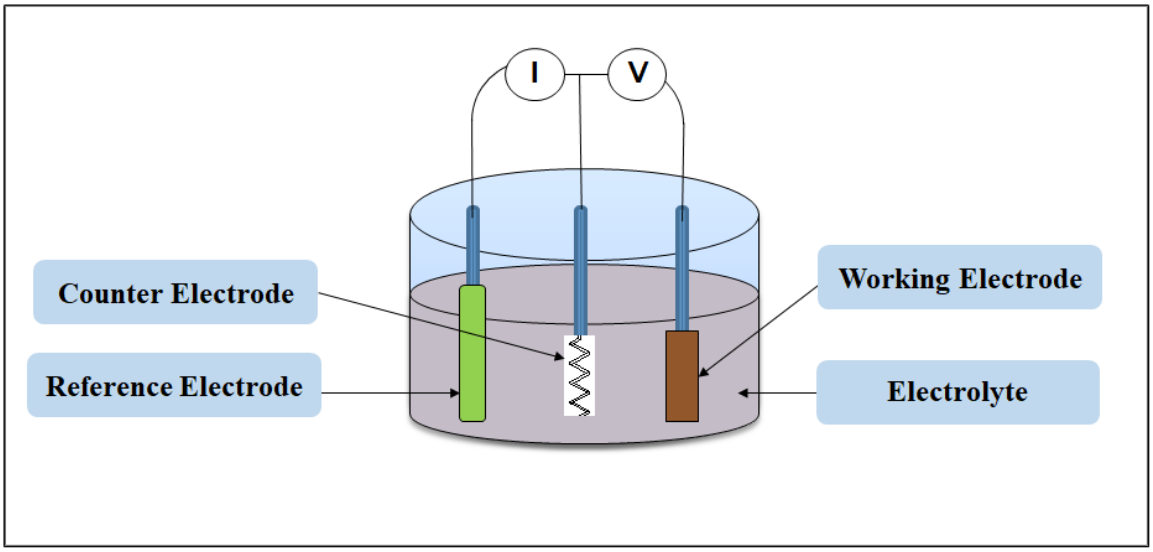

Figure 2.2: Schematic illustration of three-electrode cell system.

2.3.3.1 Electrochemical Characterizations of the Samples for Supercapacitor

In order to demonstrate the potential applications of these samples for supercapacitors, the electrochemical performances were investigated. The electrochemical performances of these samples were investigated via cyclic voltammetry, galvanostatic charge-discharge measurements, and electrochemical impedance spectroscopy. The CV technique was carried out in a potential range of 0 - 0.6 V (*vs.* SCE) at various scan rates (1-300 mV/s). The GCD measurements were performed at various current densities (0.75 – 15 mA/cm^2). The EIS analysis was also carried out in a frequency range of 0.05-10,000 Hz with an amplitude of 10 mV. An aqueous solution of 3M KOH was utilized as an electrolyte for supercapacitor measurements.

2.3.3.2 Electrocatalysts Characterizations of the Samples for Water Splitting

Oxygen evolution and hydrogen evolution reactions of these samples were also investigated using electrochemical measurements. The linear sweep voltammetry, chronoamperometry, and electrochemical impedance spectroscopy were performed to study electrocatalyst properties and potentials toward OER and HER. These investigations were carried out in an aqueous 1M KOH electrolyte. The LSV measurement for OER was carried out in a potential range of 0.14 – 0.84 V at a scan rate of 2 mV/s. In the case of HER, the potential range of -0.9 to -1.7 V at 2 mV/s scan rate was applied. The obtained potentials were all converted to the reversible hydrogen electrode (RHE) using the following equation:

$$V_{RHE} = (V_{SCE} + 1.067) - I \times R \quad \ldots\ldots\ldots\ldots\ldots (2)$$

Where the V is the potential (V), 1.067 is the standard reference electrode saturated calomel electrode used (Hg/Hg_2Cl_2), I is the current at the same potential (A), and the R is the resistance of the electrode at 0 V. The over potential of OER and HER were calculated based on the following equation:

OER, overpotential = V_{SCE} + 1.067 -1.23 ……. (3)

HER, overpotential = V_{SCE} + 1.067 ……. (4)

Whereas, the 1.23 is the theoretical potential for water splitting *vs.* RHE, in the case of HER the theoretical potential is zero *vs.* RHE.

CHAPTER III

RESULTS AND DISCUSSION

3.1 Characterizations of the Synthesized Samples

3.1.1 X-Ray Diffraction Analysis

The structure, phase purity, and crystallographic data of the synthesized samples were examined by performing X-ray diffraction analysis. **Figures 3.1-3.6** show the XRD patterns of all the synthesized samples. The $Ni(OH)_2$ samples revealed characteristic diffraction peaks of (003), (006), (101), (015), (018), and (110) at around 13°, 25°, 34°, 33°, 43°, and 60°, respectively, which can be indexed as the α-$Ni(OH)_2$ structure (JCPDS No. 38-0715) [22]. In addition, no diffraction peaks other than peaks due to $Ni(OH)_2$ could be found from the XRD patterns, indicating the high purity of the sample. The XRD patterns of NiO-CTAB and NiO-PVP exhibit three strong peaks ~ 37°, 43°, and 63°, and one weak peak at 76° corresponding to the (111), (200), (220), and (311) diffraction planes, respectively. All these observed peaks in the XRD patterns can be indexed to a cubic phase of NiO (JCPDS No. 44-1159). No peaks from other phases were observed, suggesting the phase purity and high crystallinity of the samples. The XRD patterns of NiS_2 prepared with CTAB or PVP both had the same crystal structures as the other analyzed. Also, all of the diffraction peaks (110), (101), (300), (021), (220), (211), (131), (410), (401), (321), (330), (012), (600), (042), and (031) agree well with the standard pattern of rhombohedral

crystalline NiS_2 (JCPDS 12-0041) [23]. Furthermore, the XRD patterns show no impurities, confirming the phase purity of the synthesized sample. The average crystallite size of all the samples was calculated using the Scherrer equation [24] based on the most intense peak.

$$t = \frac{0.9\lambda}{\beta \cos\theta} \quad \ldots\ldots\ldots\ldots\ldots (5)$$

Where t is the average crystallite size, λ is the X-ray wavelength, β is the full width at half maximum (FWHM) of the diffraction line, and θ is the diffraction angle of the XRD spectra. The average crystallite sizes and the FWHM for all the samples are listed on **Table 1**.

Table 1: Average crystallite size of all the synthesized samples.

Samples	***FWHM***	***Crystallite size (nm)***
$Ni(OH)_2$-CTAB	0.889	94
$Ni(OH)_2$-PVP	0.636	131
NiO-CTAB	1.566	57
NiO-PVP	1.492	60
NiS_2-CTAB	0.517	163
NiS_2-PVP	0.409	208

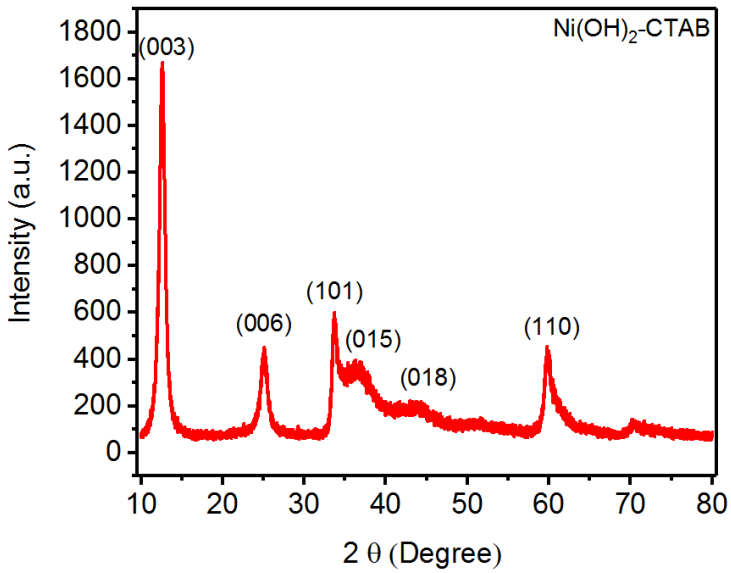

Figure 3.1: XRD patterns of $Ni(OH)_2$ synthesized using CTAB.

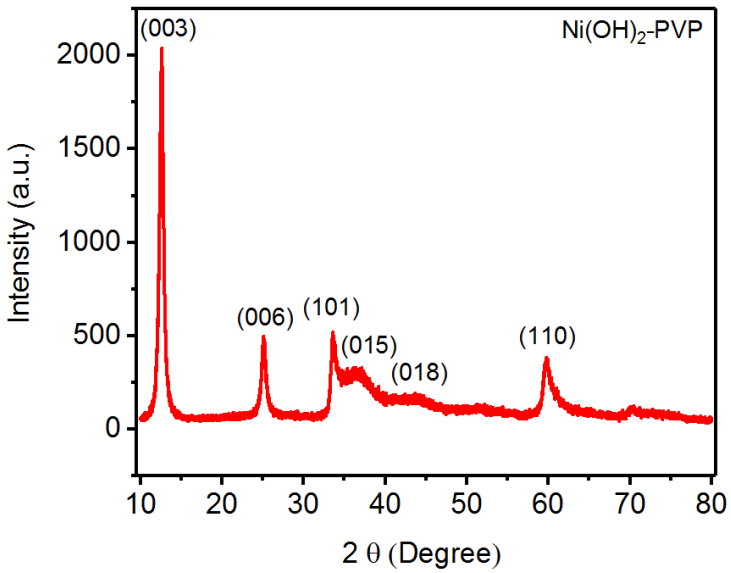

Figure 3.2: XRD patterns of $Ni(OH)_2$ synthesized using PVP.

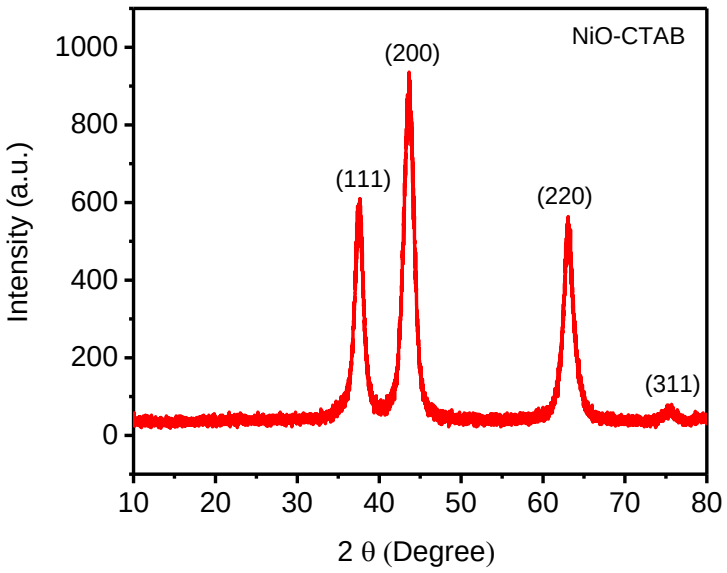

Figure 3.3: XRD patterns of NiO synthesized using CTAB.

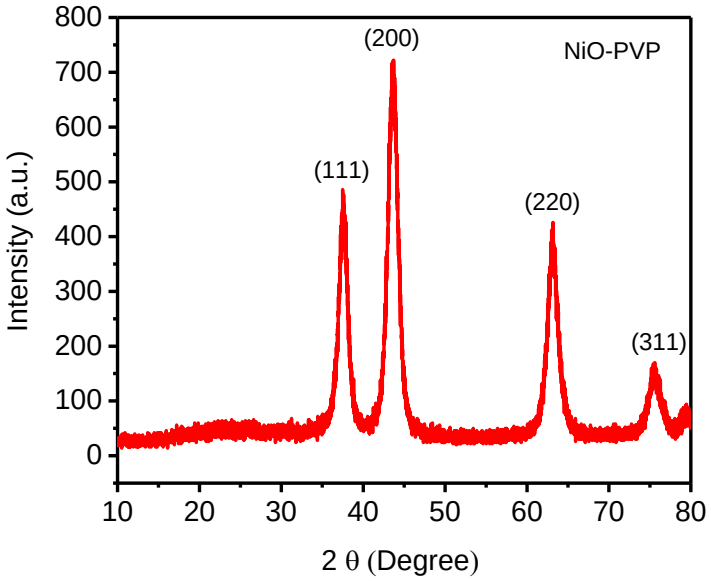

Figure 3.4: XRD patterns of NiO synthesized using PVP.

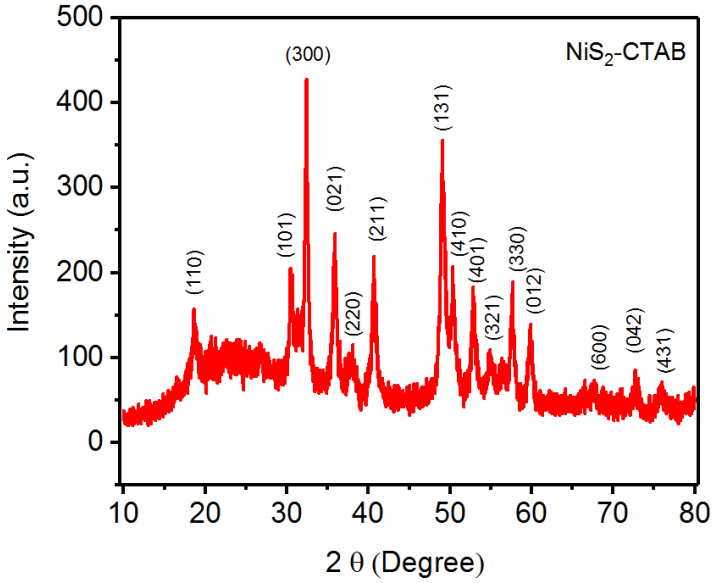

Figure 3.5: XRD patterns of NiS_2 synthesized using CTAB.

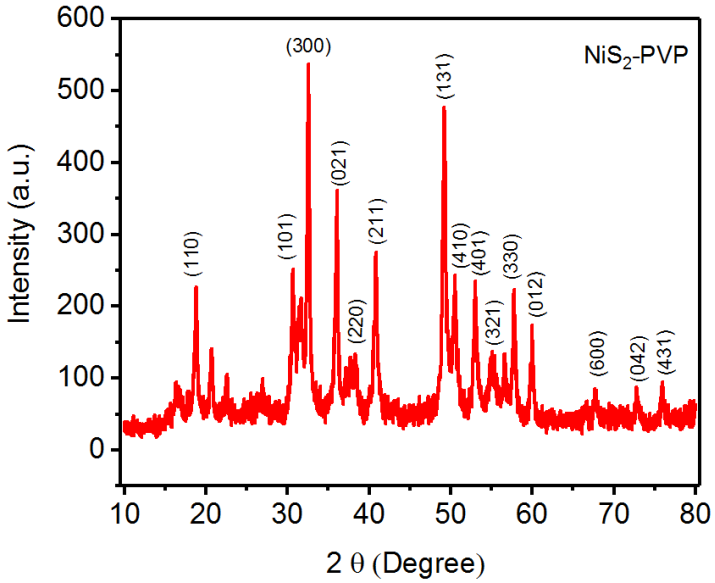

Figure 3.6: XRD patterns of NiS_2 synthesized using PVP.

3.1.2 Scanning Electron Microscopy Analysis

The morphology and structure characteristics of all the samples are further investigated in details by using SEM characterization. **Figures 3.7-3.12** show the SEM images of all the samples at different magnifications. It was observed that the morphology and the size of all the synthesized samples are highly dependent on the presence of CTAB and PVP.

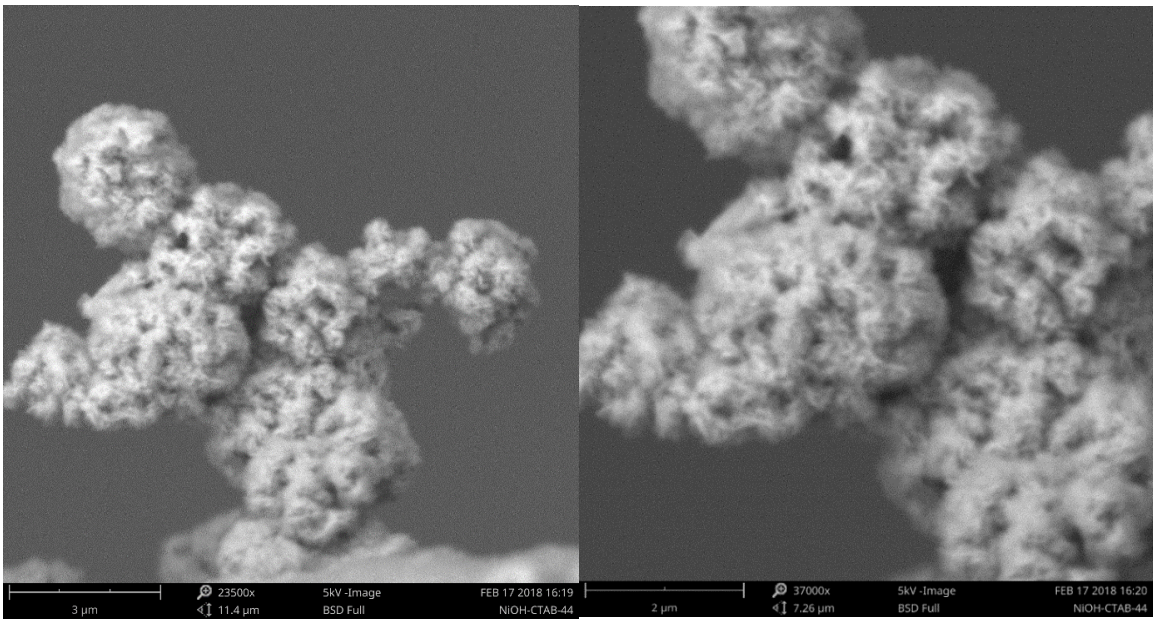

Figure 3.7: SEM image of $Ni(OH)_2$-CTAB at various magnifications.

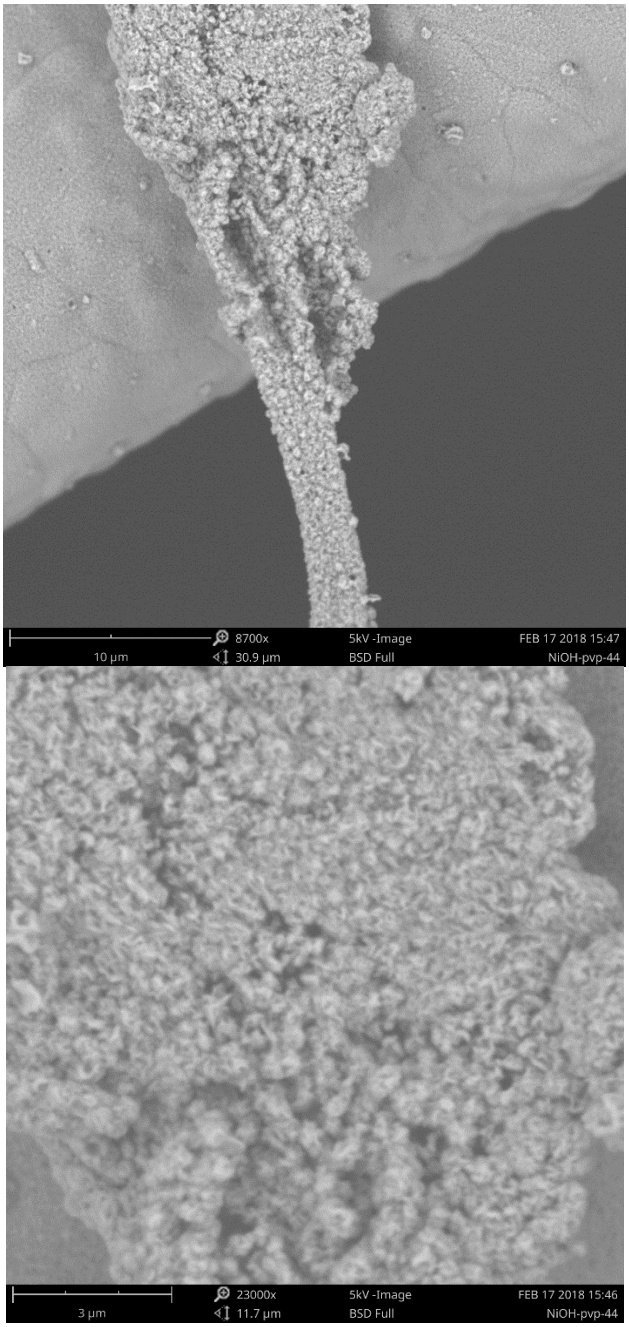

Figure 3.8: SEM image of $Ni(OH)_2$-PVP at various magnifications.

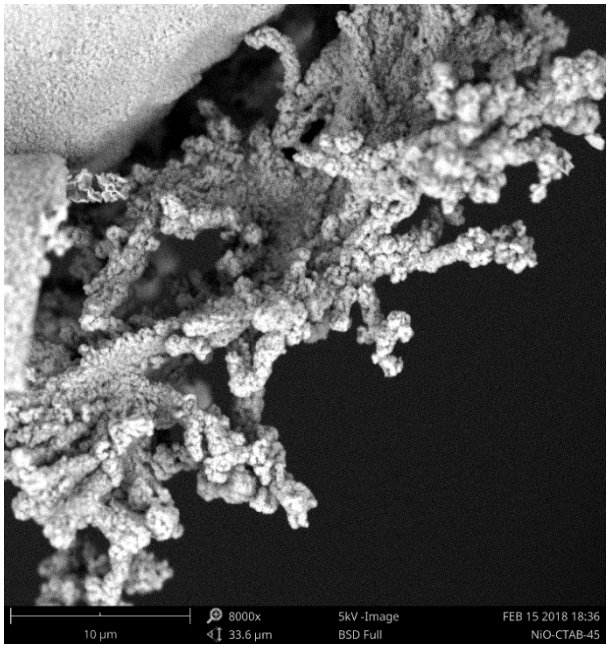

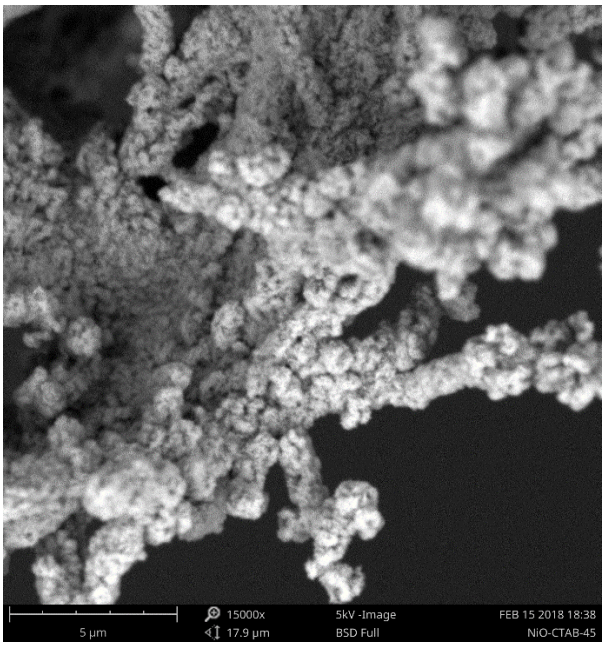

Figure 3.9: SEM image of NiO-CTAB at various magnifications.

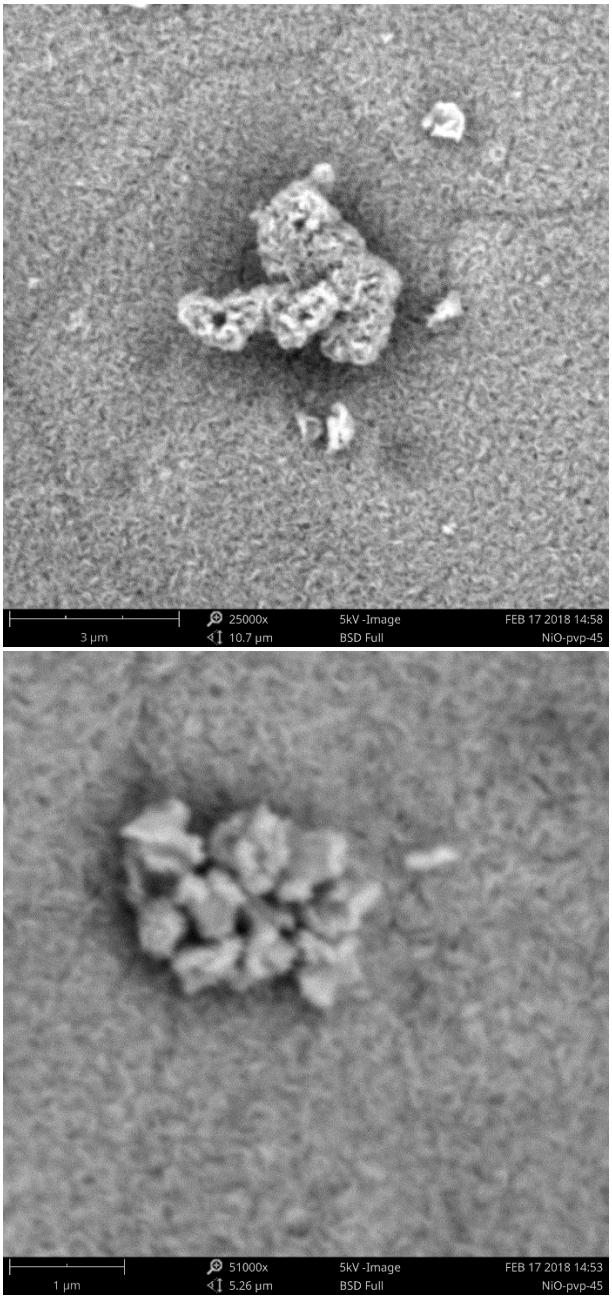

Figure 3.10: SEM image of NiO-PVP at various magnifications.

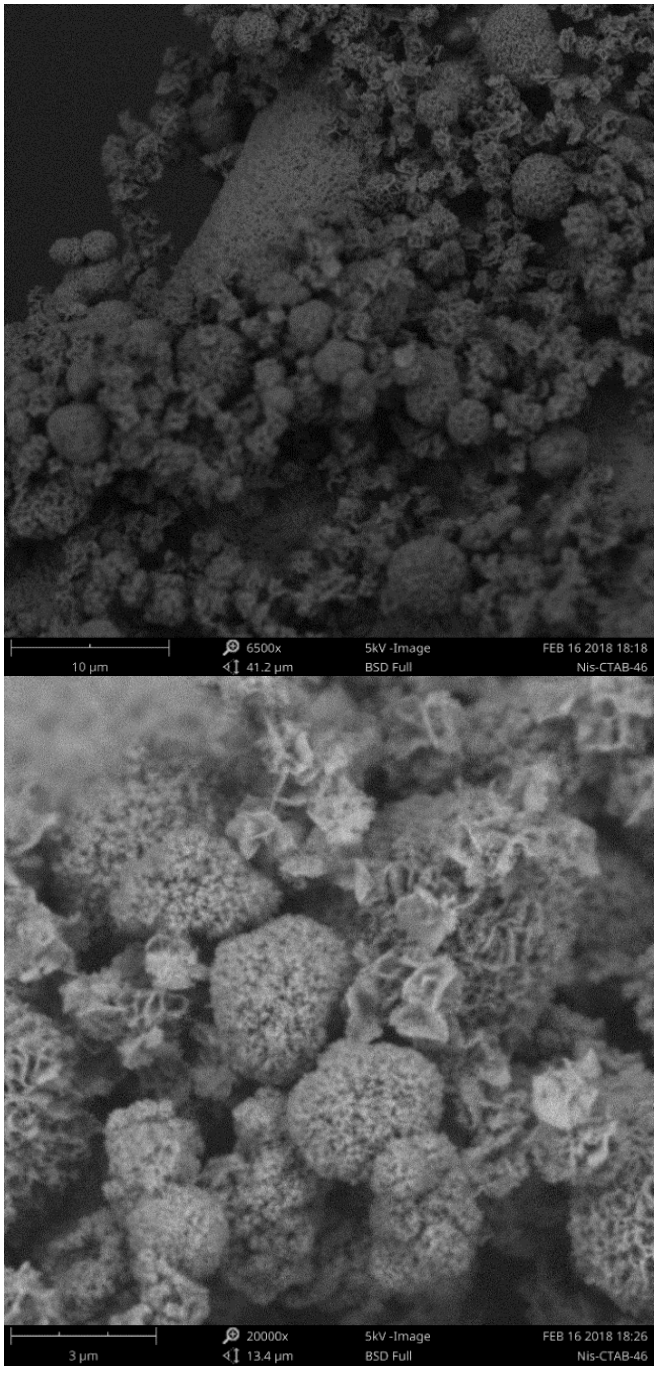

Figure 3.11: SEM image of NiS_2-CTAB at various magnifications.

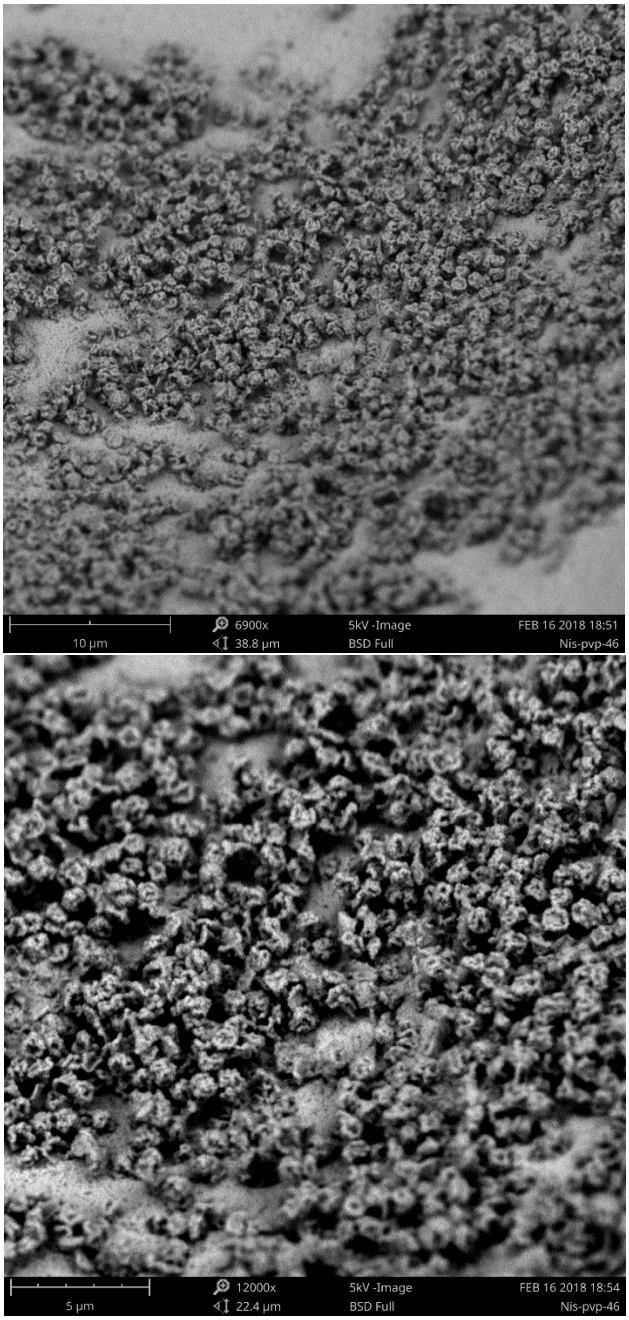

Figure 3.12: SEM image of NiS_2-PVP at various magnifications.

3.2 Electrochemical Analysis

3.2.1 Cyclic Voltammetry

Figures 3.13-3.19 show the typical cycle voltammograms for all the synthesized samples. The CV curves in each profile show a pair of redox peaks. The redox peak reveals the pseudocapacitive behavior of these electrodes which is ascribed to the reversible faradic redox reactions. From the CV curves at various scan rates, it was observed that the peak position shifts towards higher potential during the oxidation process and lower potentials during the reduction process upon increasing the scan rates from 1-300 mV/s. For example, nickel sulfide's (NiS_2-CTAB) oxidation peak was observed at ≈ 0.52 V at a scan rate of 10 mV/s, which shifted to 0.54 V at a scan rate of 20 mV/s, suggesting the process is diffusion controlled. Moreover, it was observed that the NiO and $Ni(OH)_2$ electrodes grown with the presence of CTAB and PVP showed one oxidation peak and one reduction peak during the process [25]. Whereas, the NiS_2 electrodes grown with the presence of CTAB and PVP exhibited two oxidation peaks and two reduction peaks during the process. These peaks of NiS_2 electrodes appeared clearly at low scan rates and slowly vanished at high scan rates. For instance, a pair of redox peaks of NiS_2-CTAB was observed at 0.44 V and 0.54 V, respectively, at a scan rate of 20 mV/s. For NiS_2-PVP, they were observed at 0.45 V and 0.58 V, respectively, at the same scan rate. These currents could be ascribed to the further oxidation of sulfides. For example, Zhang, *et. al.*, have synthesized a NiS_2 hierarchical flower via a solvothermal method, and reported a pair of redox peaks at 0.4 V and 0.5 V at a scan rate 100 mV/s [26].

The following reactions give an explanation for the mechanism of the all electrode redox processes in KOH electrolyte:

$Ni(OH)_2 + OH^- \leftrightarrow NiOOH + H_2O + e^-$,

$NiO + OH^- \leftrightarrow NiOOH + e^-$,

$NiS_2 + OH^- \leftrightarrow NiS_2\text{-}OH + e^-$, [26]

Furthermore, the CV integral area under the curve was observed to depend on CTAB and PVP during the synthesis. Also, it showed remarkable improvement after converting to NiS_2. The increase in the integrated area under the curve implied how much more charge can be stored. For example, at a scan rate of 50 mV/s, the NiO-PVP, $Ni(OH)_2$-PVP, and NiS_2-PVP area is, 62, 176, and 406 mC, respectively. In comparison, the estimated area of NiO-CTAB, $Ni(OH)_2$-CTAB, and NiS_2-CTAB is 88, 183, and 508 mC, respectively. The noticeable improvement could be attributed to the morphological structure. As a result, the CV of NiS_2-CTAB at a scan rate of 50 mV/s possessed the largest area indicating its highest energy storage capacity owing to the high electrochemical activity of NiS_2. Besides, the CV profile remains similar even at the high scan rate of 50 mV/s, implying excellent rate performance and chemical stability.

The CV measurements were also used to calculate the specific capacitance of the synthesized electrodes as a function of scan rate. The specific capacitance was calculated according to the following equation:

$$C_{sp} = \frac{Q}{\Delta V \times (\frac{\partial v}{\partial t}) \times A} \quad \ldots\ldots\ldots\ldots\ldots (6)$$

Where:

Q is the integrated area under the CV curve (mC), ΔV is the potential window (V), $\partial v/\partial t$ is the scan rate, and A is the area of the applied electrodes (cm^2).

Figure 3.20 illustrates the variation in specific capacitance as a function of scan rates for all the electrodes. It can be observed that specific capacitance decreases when a scan rate increases. This correlation could be ascribed to the insufficient time for redox reactions to occur at higher scan rates. For more clarification, at a higher scan rate, the ion concentration at the electrode/electrolyte interface increases rapidly, and the diffusion rate of electrolyte from electrode/electrolyte interface to electrode will be not enough to satisfy the electrochemical reactions [27]. As observed, the specific capacitance of 2,312 mF/cm^2 exhibited by NiS_2-CTAB at a scan rate of 20 mV/s is higher than other prepared electrodes in this study. The specific capacitance of 166, 271, 648, 720, 2,241, and 2,312 mF/cm^2 for NiO-PVP, NiO-CTAB, $Ni(OH)_2$-PVP, $Ni(OH)_2$-CTAB, NiS_2-PVP, and NiS_2-CTAB, respectively, were observed at a scan rate of 20 mV/s. The specific capacitances of all the synthesized electrodes are listed in **Table 2**.

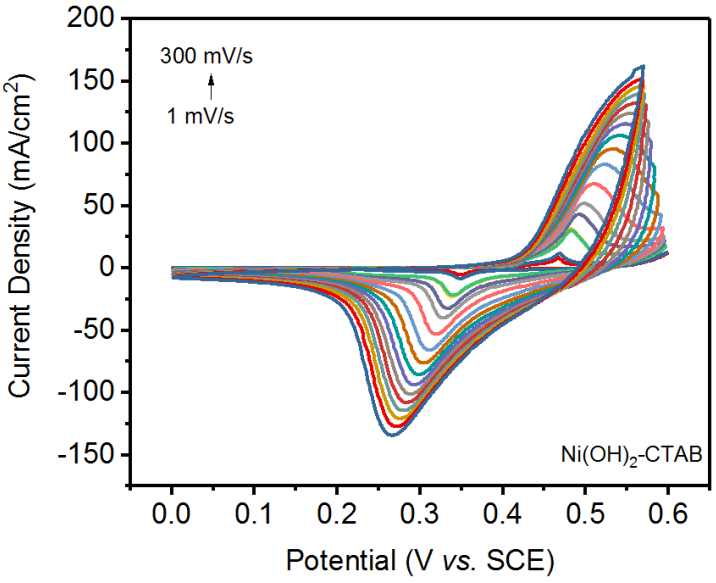

Figure 3.13: CV curves of $Ni(OH)_2$-CTAB sample at various scan rates.

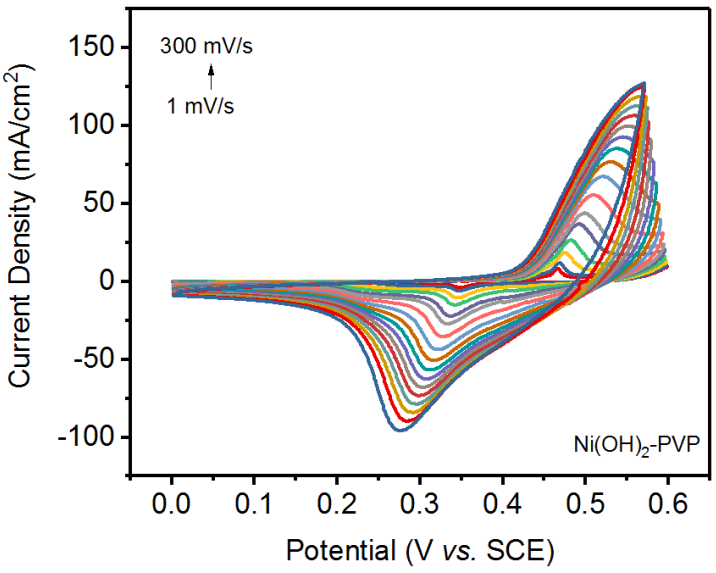

Figure 3.14: CV curves of $Ni(OH)_2$-PVP sample at various scan rates.

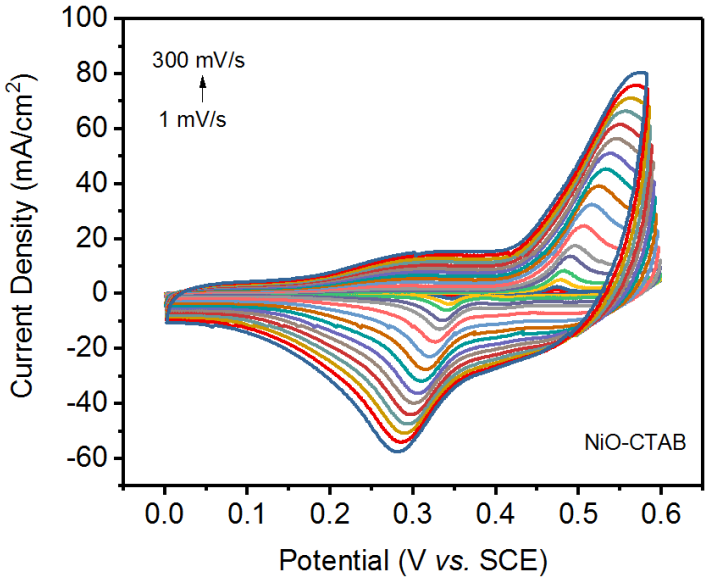

Figure 3.15: CV curves of NiO-CTAB sample at various scan rates.

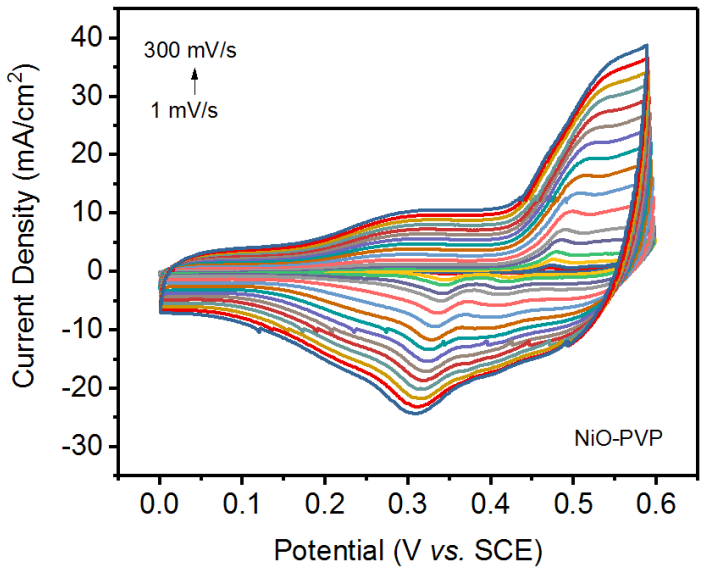

Figure 3.16: CV curves of NiO-PVP sample at various scan rates.

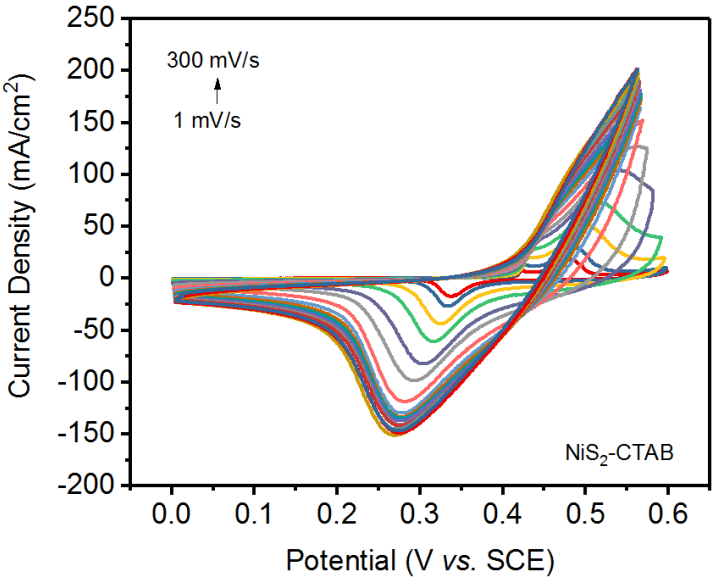

Figure 3.17: CV curves of NiS_2-CTAB sample at various scan rates.

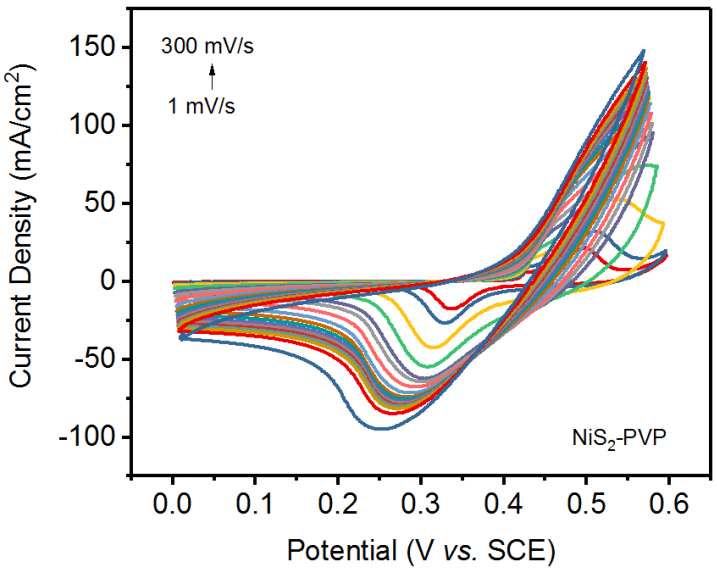

Figure 3.18: CV curves of NiS_2-PVP sample at various scan rates.

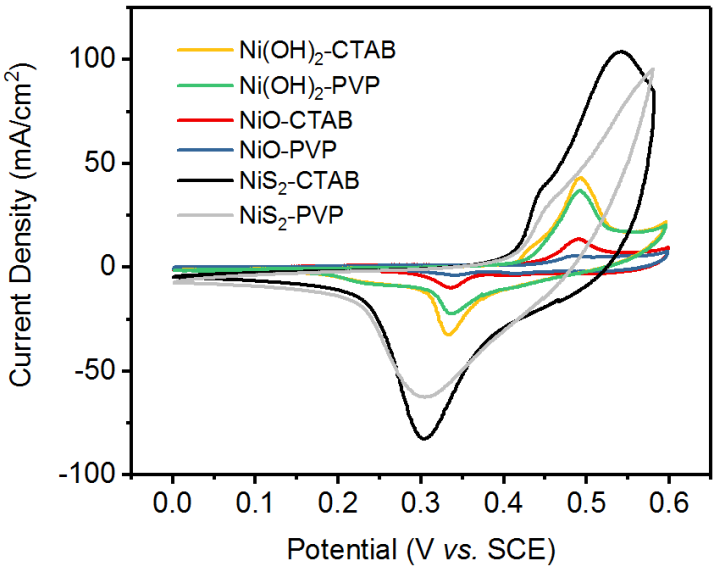

Figure 3.19: Comparative CV curves at a scan rate of 20 mV/s.

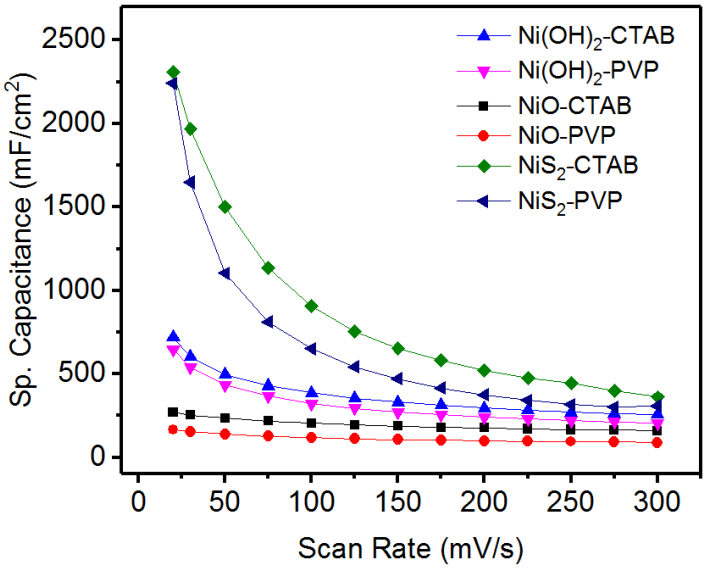

Figure 3.20: The variation of specific capacitance as a function of scan rate for all the synthesized electrodes.

Table 2: Specific capacitance of all the synthesized electrodes at a scan rate of 20 mV/s.

Electrode	*Specific Capacitance (mF/cm^2)*
NiS_2-CTAB	2,312
NiS_2-PVP	2,241
$Ni(OH)_2$-CTAB	720
$Ni(OH)_2$-PVP	648
NiO-CTAB	271
NiO-PVP	166

3.2.2 Galvanostatic Charge-Discharge Analysis

The charge storage capacity of all the samples was further investigated using galvanostatic charge and discharge measurements. **Figures 3.21-3.27** illustrate the GCD characteristics of all the electrodes at various current densities. It was observed that the GCD curves are nearly symmetrical at all current densities, referring to the high electrochemical reversibility of the samples [27]. In additional to the above, the discharge time appeared to decrease with the increase of the current density. That can be expounded by the diffusion effect limiting the diffusion and movement of electrolyte ions OH^- within the electrodes at a high discharge current density [28,29]. It was observed that the GCD obtained results of the NiO, $Ni(OH)_2$, and NiS_2 samples synthesized using CTAB are higher than those synthesized using PVP. For instance, the discharge time of the samples synthesized using CTAB is longer than the other samples synthesized using PVP at different current densities. As an example, the discharge time of 33, 279, and 1149 sec was observed for NiO-CTAB, $Ni(OH)_2$-CTAB, and NiS_2-CTAB at a current density of 2 mA/cm^2, respectively, while discharge times of 21, 183, and 580 sec were observed for NiO-PVP, $Ni(OH)_2$-PVP, and NiS_2-PVP at the corresponding current density, respectively. Briefly, the discharge curves of NiS_2-CTAB display the longest time, indicating its highest specific capacitance among all the samples in this study. Furthermore, the areal specific capacitance of all the samples was calculated from galvanostatic discharge curves as a function of current density according to the following equation [8]:

$$C_s = \frac{I \times \Delta t}{A \times \Delta V} \quad \ldots\ldots\ldots\ldots\ldots (7)$$

Where:

Cs is the areal specific capacitance (mF/cm^2), *I* is the discharge current applied to the electrode (mA), Δt is the discharge time from high to low potential (s), *A* is the area of the applied electrode (cm^2), and ΔV is the potential window (V). **Figure 3.28** presents the areal specific capacitance of all the samples at different current densities. It was observed that the areal specific capacitance of the samples decreases with increasing discharge current. The effect of the decrease in the areal capacitance with the increase of the discharge current could be ascribed to the increase of potential drop and insufficient faradic redox reaction at higher discharge currents [27]. Furthermore, the energy storage capacity was observed to depend on the presence of PVP and CTAB during the synthesis. It was observed that the areal capacitance of NiO improved significantly after converting to NiS_2. An areal specific capacitance of 67, 859, and 2,633 mF/cm^2 was observed for NiO, $Ni(OH)_2$, and NiS_2 synthesized in the presence of CTAB, respectively. In contrast, the areal specific capacitance for NiO, $Ni(OH)_2$, and NiS_2 synthesized in the presence of PVP was observed to be 50, 529, and 1,211 mF/cm^2, respectively. Remarkably, the as-prepared NiS_2-CTAB sample displayed the highest areal capacitance of 2633, 2248, 1895, 1790, 1623, and 1384 mF/cm^2 at current density values of 0.75, 2, 5, 7, 10, and 15 mA/cm^2, respectively. Furthermore, the specific capacitance of NiS_2-CTAB sample can still keep up to 52.54% of the initial value (2,633 at 0.75 mA/cm^2) even at a high current density of 15 mA/cm^2. However, Weihua, *et. al.*, have recently synthesized graphene fibers coated by $NiCo_2S_4$ nanoparticles using solvothermal deposition method, which provided an areal specific capacitance of 568 mF/cm^2 at a current density of 0.5 mA/cm^2 [30]. Liu, *et. al.*, synthesized Ni_3S_2 on nickel foam and the areal specific capacitance reached was 29.4

mF/cm^2 at a current density of 20 mA/cm^2 [31]. The areal capacitances of all the synthesized electrodes are listed in **Tables 3 and 4**. The significant improvement in the charge storage capacity was due to the high electrochemical activity of NiS_2. Our studies indicate that electrochemical properties of nickel compounds are dependent on the phase of nickel compounds.

Table 3: The areal specific capacity of all the synthesized electrodes at 0.75 mA/cm^2 current density.

Electrode	***Specific Capacitance (mF/cm^2)***
NiS_2-CTAB	2,633
NiS_2-PVP	1,211
$Ni(OH)_2$-CTAB	859
$Ni(OH)_2$-PVP	529
NiO-CTAB	67
NiO-PVP	50

Table 4. Comparison of areal specific capacitance with other results.

Electrode	***Specific Capacitance (mF/cm^2)***
NiS_2-CTAB	2,312
GF/$NiCo_2S_4$	568
Ni_3S_2	29.4

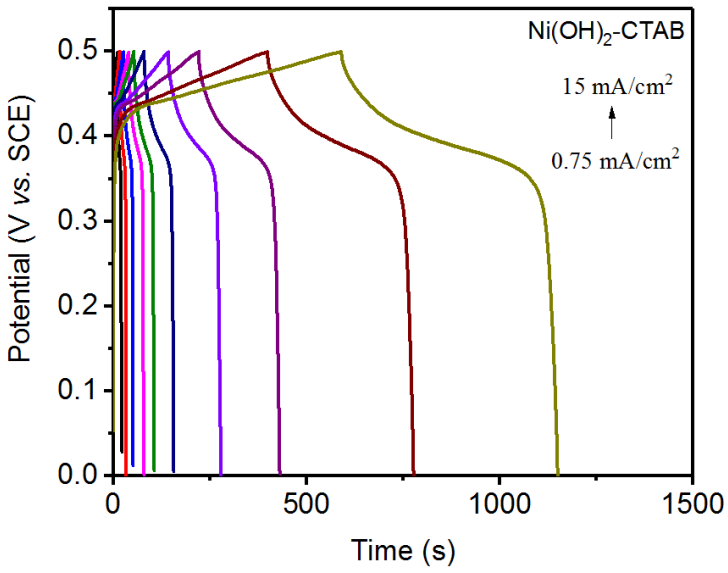

Figure 3.21: GCD plots at various current densities of $Ni(OH)_2$-CTAB on nickel foam.

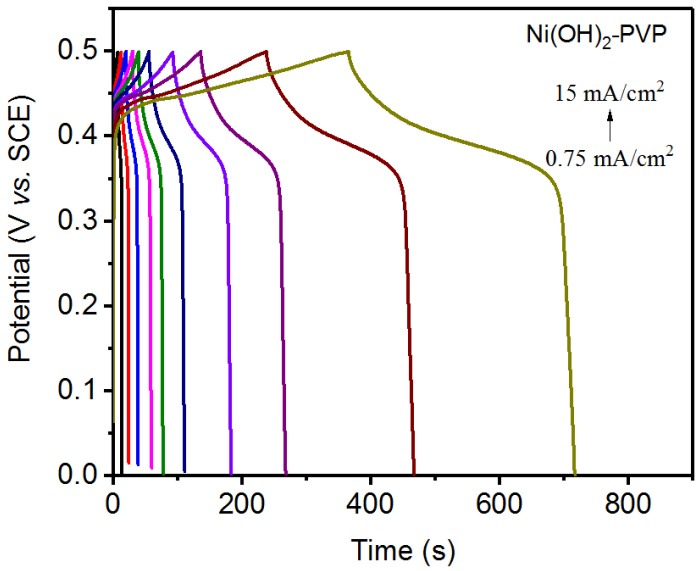

Figure 3.22: GCD plots at various current densities of $Ni(OH)_2$-PVP on nickel foam.

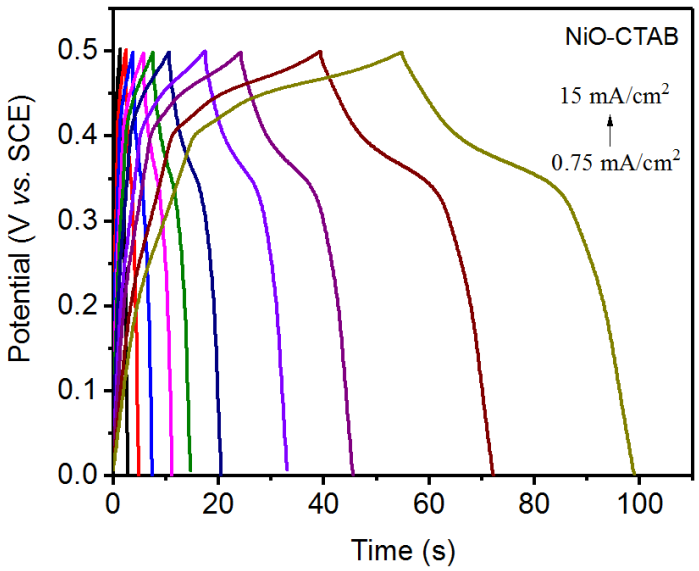

Figure 3.23: GCD plots at various current densities of NiO-CTAB on nickel foam.

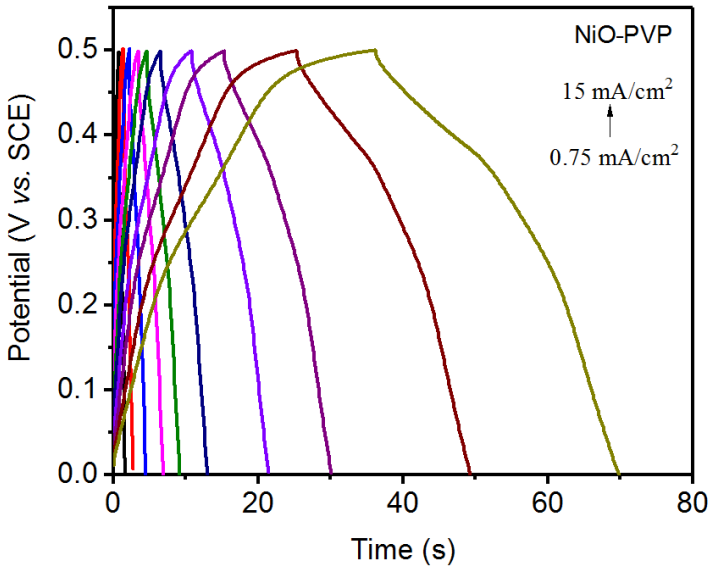

Figure 3.24: GCD plots at various current densities of NiO-PVP on nickel foam.

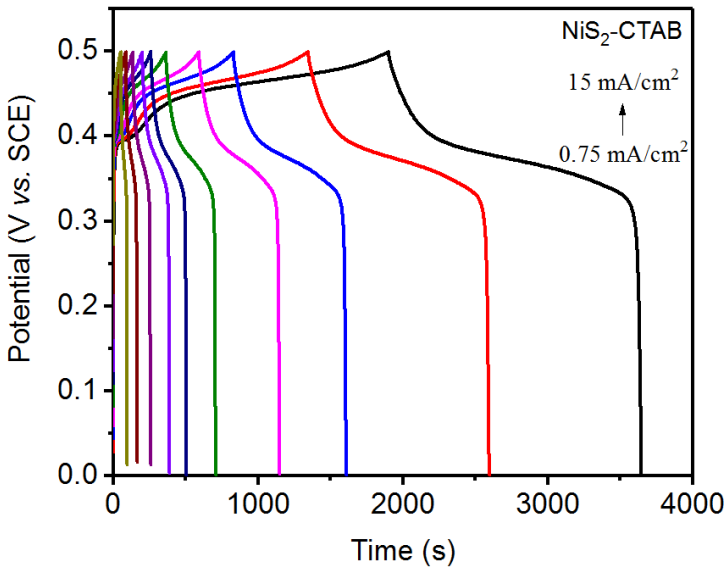

Figure 3.25: GCD plots at various current densities of NiS_2-CTAB on nickel foam.

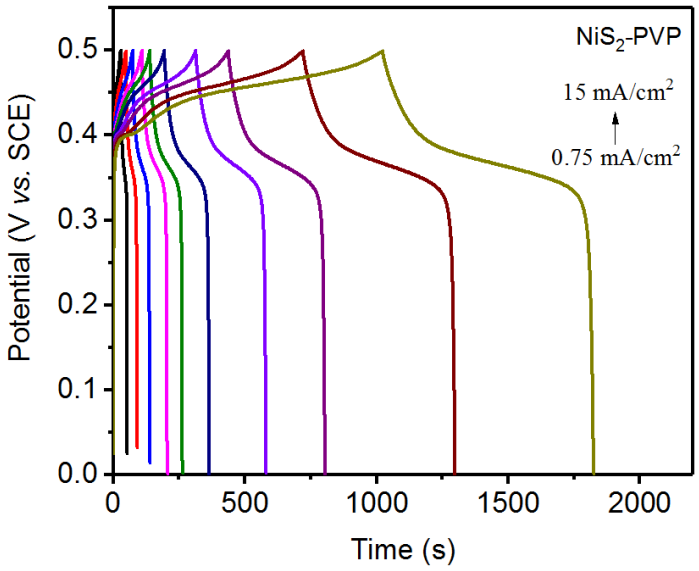

Figure 3.26: GCD plots at various current densities of NiS_2-PVP on nickel foam.

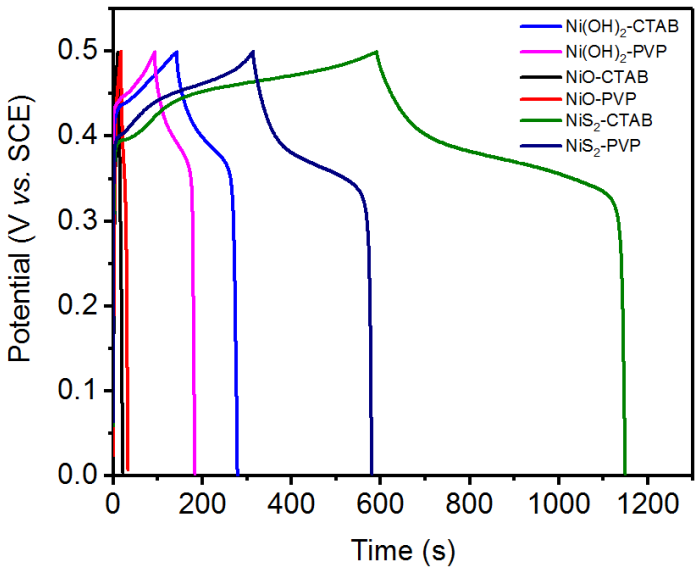

Figure 3.27: GCD profile for all the samples at a current density of 2 mA/cm^2.

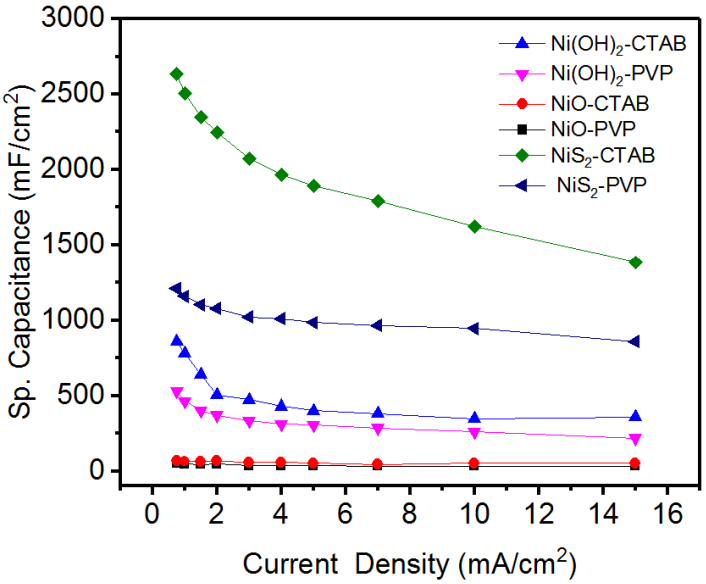

Figure 3.28: The areal specific capacitance of all the samples at various current densities.

3.2.3 Electrochemical Impedance Spectroscopy Analysis

Figures 3.29-3.30, present Nyquist plots of the electrodes and the impedance as a function of frequency at 0 V *vs*. Hg/Hg_2Cl_2. The charge transfer resistance and diffusion resistance of NiS_2-CTAB are lower than the other electrodes, indicating its fast electrolyte ions diffusion during the redox process. The NiS_2-CTAB electrode showed the lowest resistance of ~ 2.5 Ω among all the electrodes.

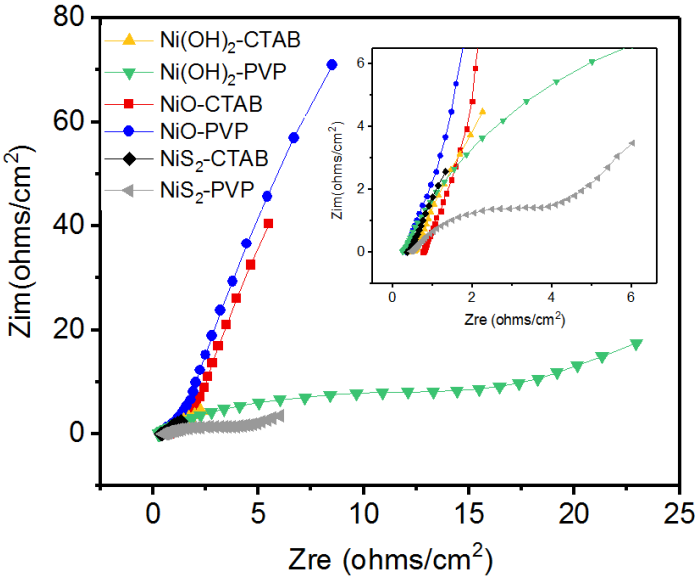

Figure 3.29: Nyquist plots of all the electrodes at 0 V *vs*. Hg/Hg_2Cl_2 (inset figure shows a zoom picture).

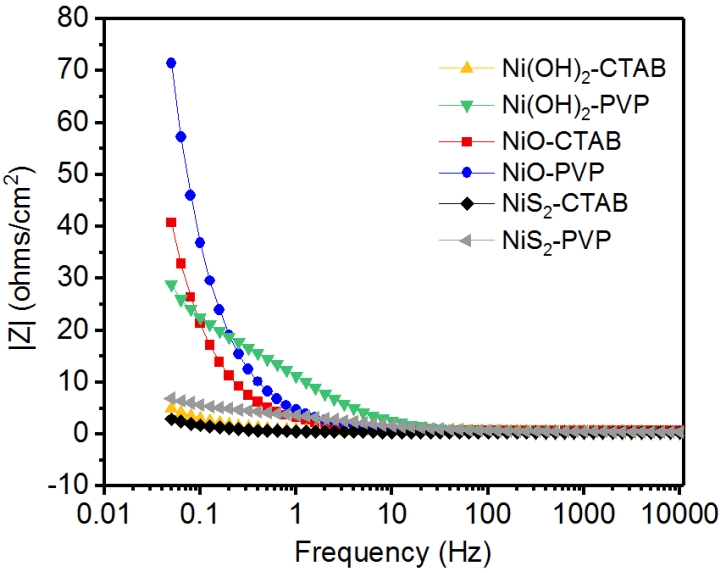

Figure 3.30: Impedance as a function of frequency for all the electrodes at 0 V *vs.* Hg/Hg_2Cl_2.

3.3 Electrocatalyst Analysis for Water Splitting

3.3.1 Electrocatalyst for Oxygen Evolution Reaction

The electrocatalytic performances of all the electrodes were investigated in an alkaline solution of 1M KOH for the oxygen evolution reaction. **Figure 3.31-3.32**, illustrate the OER polarization curves of $Ni(OH)_2$-CTAB, $Ni(OH)_2$-PVP, NiO-CTAB, NiO-PVP, NiS_2-CTAB, and NiS_2-PVP grown on nickel foam. The NiS_2-CTAB electrode exhibited the lowest overpotential of 298 mV compared with other electrodes of $Ni(OH)_2$-CTAB, $Ni(OH)_2$-PVP, NiO-CTAB, NiO-PVP, and NiS2-PVP. The overpotentials for $Ni(OH)_2$-CTAB, $Ni(OH)_2$-PVP, NiO-CTAB, NiO-PVP, NiS_2-CTAB, and NiS_2-PVP were observed to be 303, 337, 339, 353, 298, and 301 mV at 10 mA/cm^2, respectively. However, the NiS_2-CTAB electrode performance was noticed to suffer at high current densities, and the overpotential was observed to increase with the increase of the current densities. While the $Ni(OH)_2$-CTAB shows a very stable level event at high current densities among all the electrodes in this study. Moreover, based on the definition of the onset potential, which is the minimum potential required to achieve the current density of 1 mA/cm^2, the following results were obtained [21]. The onset potentials of 235, 257, 281, 292, 245, and 251 mV were observed for $Ni(OH)_2$-CTAB, $Ni(OH)_2$-PVP, NiO-CTAB, NiO-PVP, NiS_2-CTAB, and NiS_2-PVP respectively. The Tafel slopes of the mentioned electrodes were further determined via LSV curves, as seen in **Figure 3.33**. The $Ni(OH)_2$-CTAB electrode showed the lowest result for a Tafel slope of 48 mV per decade among the investigated electrodes in this study. Meanwhile, the other electrodes $Ni(OH)_2$-PVP, NiO-CTAB, NiO-PVP, NiS_2-CTAB, and NiS_2-PVP exhibited relatively satisfactory Tafel slopes of 63, 58, 57, 111, and 115 mV per decade, respectively. To compare with other research results, Lv, *et. al*., have

synthesized hollow mesoporous $NiCo_2O_4$ nanocages and reported an overpotential of 340 mV at a current density of 10 mA/cm^2 with a Tafel slope of 75 mV/dec [5]. Zhen, *et. al*., prepared nickel oxide nanoflakes by a hydrothermal method and examined its activity for OER. The NiO(NFs) displayed OER overpotential of 350 mV and a Tafel slope of 97.4 mV/dec at 10 mA/cm^2 current density [32]. Zhou, *et. al*., prepared AuNCs@$Co(OH)_2$ and AuNCs@$Ni(OH)_2$ core shell and studied its electrocatalytic performance for OER. The overpotential of 350 and 375 mV in 1M KOH were obtained at a current density of 10 mA/cm^2, respectively [33]. Zhou, *et. al*., synthesized multi-walled carbon nanotubes MWCNTs/$Ni(OH)_2$ using a hydrothermal method and reported an OER overpotential of 470 mV with the Tafel slope of 87 mV/dec at 10mA/cm^2 [32]. In addition, Han, *et. al.*, reported an overpotential for NiO/Ni foam of 390 mV at 10 mA/cm^2 [35]. The overpotentials of the electrodes at a current density of 10 mA/cm^2 and the corresponding Tafel slopes are listed in **Tables 5 and 6**.

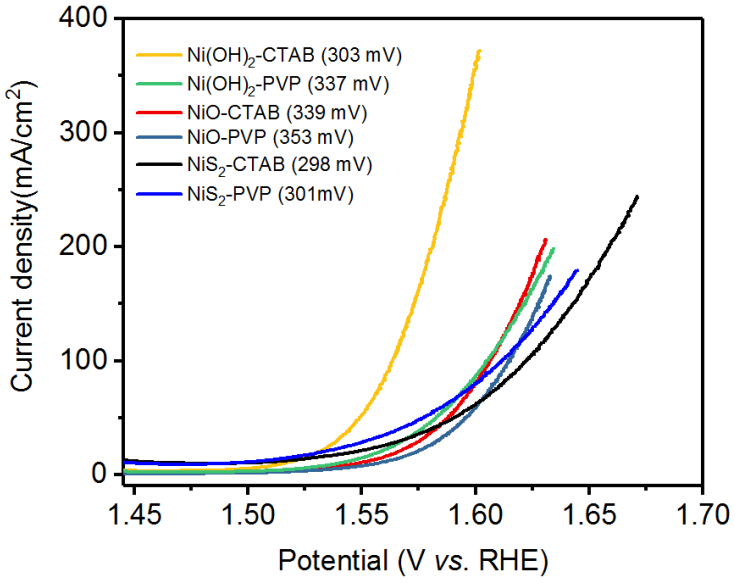

Figure 3.31: LSV polarization curves for all the electrodes.

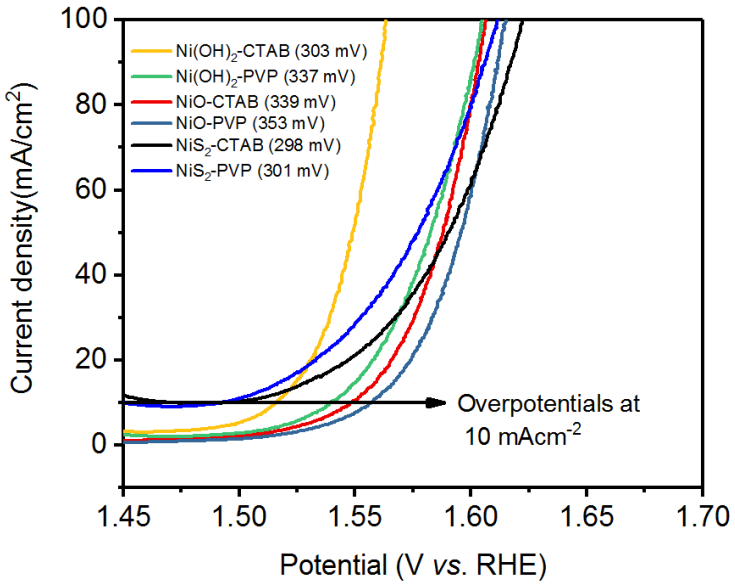

Figure 3.32: LSV polarization curves for all electrodes (zoomed).

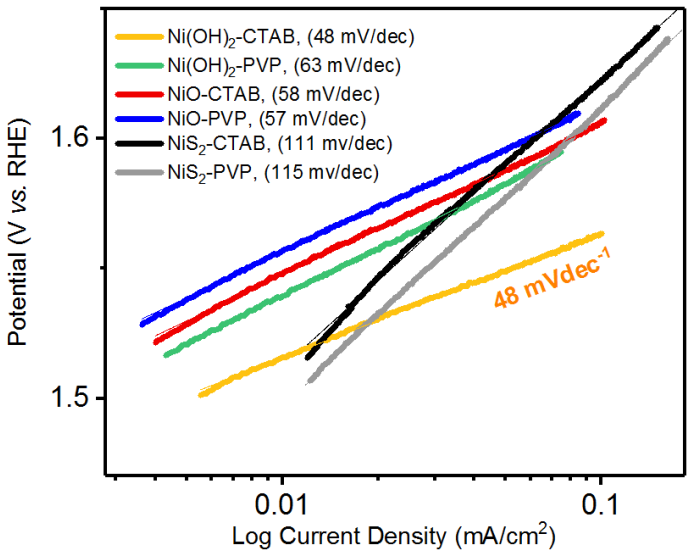

Figure 3.33: Represent the corresponding Tafel slopes.

Table 5: The OER overpotentials of all the synthesized electrodes at a current density of 10 mA/cm^2 and the corresponding Tafel slopes.

Electrode	*Overpotential (mV)*	*Tafel Slope (mV/dec)*
$Ni(OH)_2$-CTAB	303	48
$Ni(OH)_2$-PVP	337	63
NiO-CTAB	339	58
NiO-PVP	353	57
NiS_2-CTAB	298	111
NiS_2-PVP	301	115

Table 6: Results of OER electrodes at 10 mA/cm^2 of other reports.

Electrode	*Overpotential (mV)*	*Tafel Slope (mV/dec)*
MWCNTs/$Ni(OH)_2$	470	87
$NiCo_2O_4$	340	75
NiO(NFs)	350	97
$Zn_xCo_{3-x}O_4$	320	52

Moreover, the electrochemical impedance spectroscopy measurements were also carried out for the investigation of charge transfer resistance R_{ct} of the electrodes. **Figures 3.34-3.37** illustrate the Nyquist plots and the impedance as a function of frequency for the electrodes at various potentials (V *vs.* Hg/Hg_2Cl_2). The behavior of Nyquist plots was observed to depend on the applied potentials. As illustrated in the figures, at the lower potential of 0V, the obtained electrodes showed as a straight line in the low-frequency region. Among the investigated electrodes in this study, the $Ni(OH)_2$-CTAB showed a low resistance of 6 Ω at 0V. The straight lines in the low-frequency region were found to start converting into a semicircle shape when increasing the potential. For instance, at a potential value of 0.5 V, the Nyquist plots of all the electrodes appeared like a semicircle. For example, the $Ni(OH)_2$-CTAB shows an apparent semicircle in the low-frequency region among the other electrodes. Resistance of 1.3, 3.2, 4, 3, 2, and 2.8 Ω was observed at 0.5 V for $Ni(OH)_2$-CTAB, $Ni(OH)_2$-PVP, NiO-CTAB, NiO-PVP, NiS_2-CTAB, and NiS_2-PVP electrodes, respectively. The superior performance of the $Ni(OH)_2$-CTAB electrode can be attributed to a smaller value of the charge transfer resistance (R_{ct}). This smaller value of R_{ct} leads to a faster electrochemical reaction rate [36].

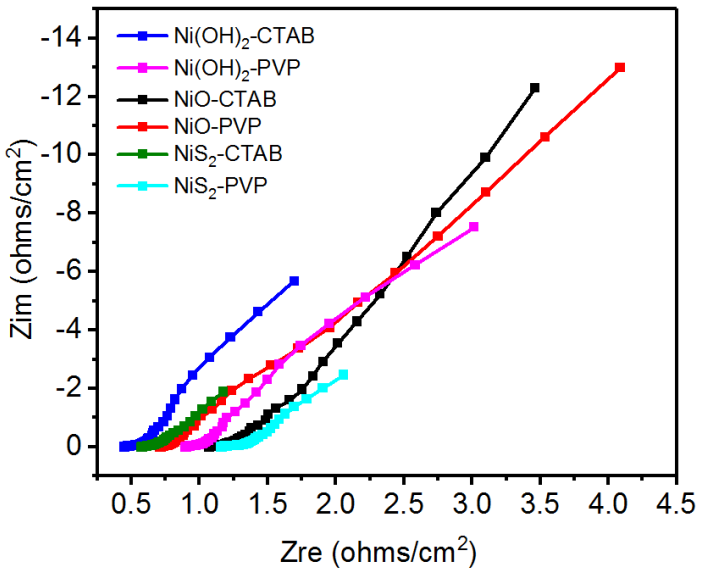

Figure 3.34: Nyquist plots of all the catalyst electrodes at 0 V *vs.* Hg/Hg_2Cl_2.

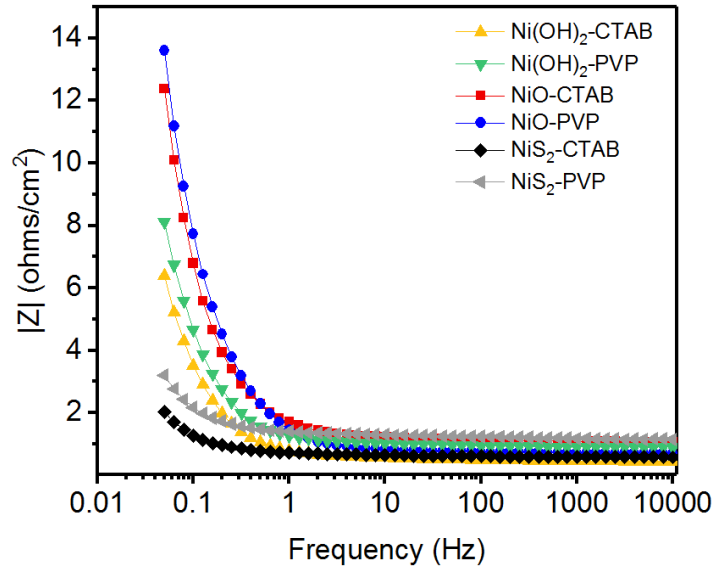

Figure 3.35: Impedance as a function of frequency for all the catalyst electrodes at 0 V *vs.* Hg/Hg_2Cl_2.

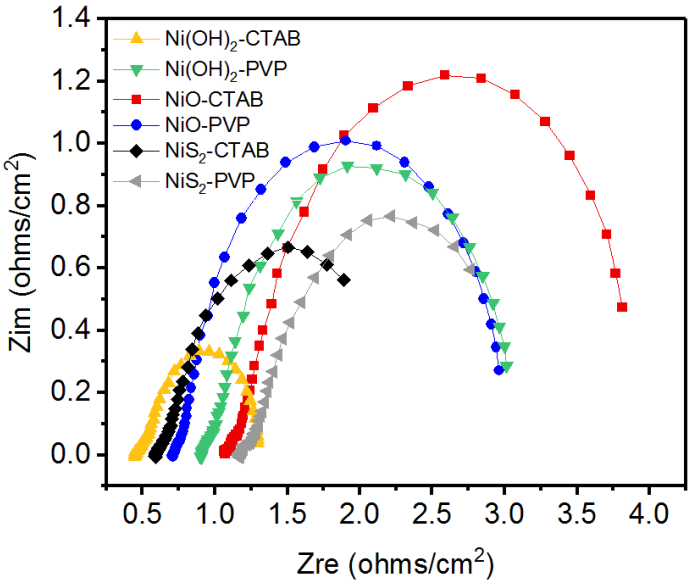

Figure 3.36: Nyquist plots of all the catalyst electrodes at 0.5 V *vs.* Hg/Hg_2Cl_2.

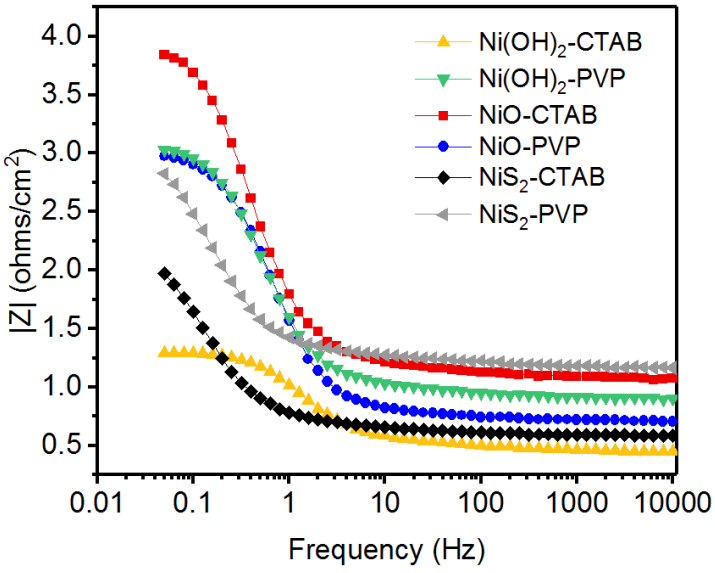

Figure 3.37: Impedance as a function of frequency for all the catalyst electrodes at 0.5 V *vs.* Hg/Hg_2Cl_2.

The long-term stability test was performed for the $Ni(OH)_2$-CTAB electrode. **Figures 3.38-3.48** represent the LSV curves, chronoamperometry, and EIS measurements for the $Ni(OH)_2$-CTAB electrode at different cycles. The $Ni(OH)_2$-CTAB electrode showed a very stable performance up to the 1000^{th} cycle, and the overpotential was noticed to decrease with cycles. The overpotential of 286 mV was noticed at the 1000^{th} cycle, showing a decrease in the overpotential between the initial cycle and the 1000^{th} cycle of 17 mV at 10 mA/cm^2. The chronoamper was also performed to further examine the stability of the $Ni(OH)_2$-CTAB electrode. The current density was almost constant for over 20 h of study as shown in **Figures 3.48**. The Nyquist plots and the impedance as a function of frequency for the electrode before and after the stability test at a potential of 0 and 0.55 (V *vs.* Hg/Hg_2Cl_2) are shown in **Figures 3.40-3.47**. The impedance was observed to decrease after the stability test. The impedance of 6 at 0 V decreased to 4.5 Ω, while the impedance of 1.3 at 0.55 V decreased to 0.8 Ω.

The high performance of the $Ni(OH)_2$-CTAB electrode could be attributed to its morphological structure, which facilitates the electrolyte to access the entire surface area of the electrode. In addition to the structured morphology, the direct growth of the $Ni(OH)_2$-CTAB on nickel foam and the binder-free approach promote a reduction in the series resistance. From all the obtained results, it can be suggested that $Ni(OH)_2$-CTAB could be utilized as a high performance and fixable materials for OER electrode.

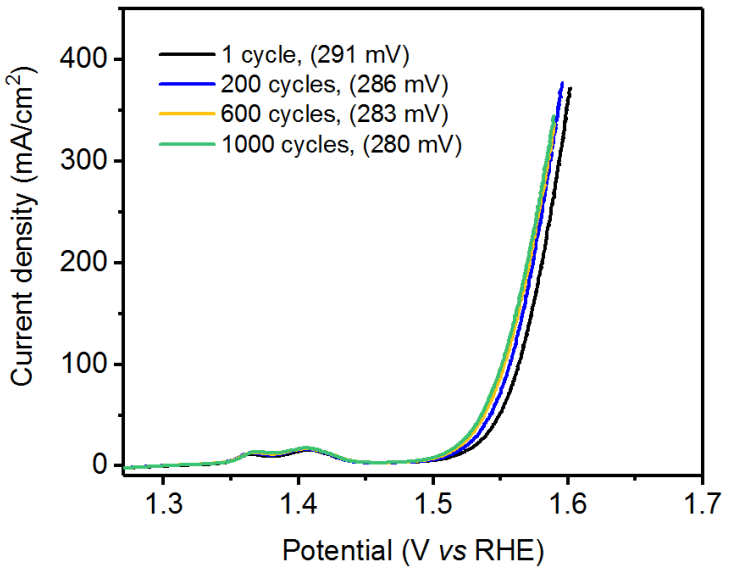

Figure 3.38: LSV polarization curves for $Ni(OH)_2$-CTAB at various cycles.

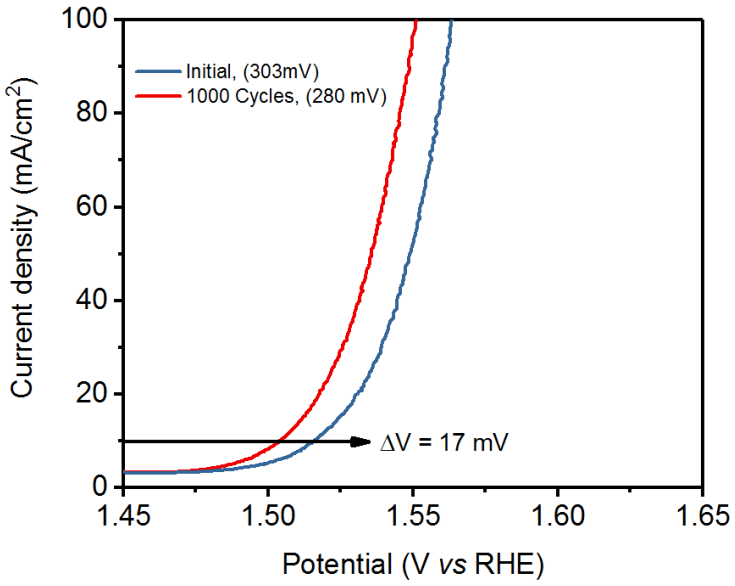

Figure 3.39: LSV polarization curves for $Ni(OH)_2$-CTAB for the initial cycle and the 1000^{th} cycles (zoomed).

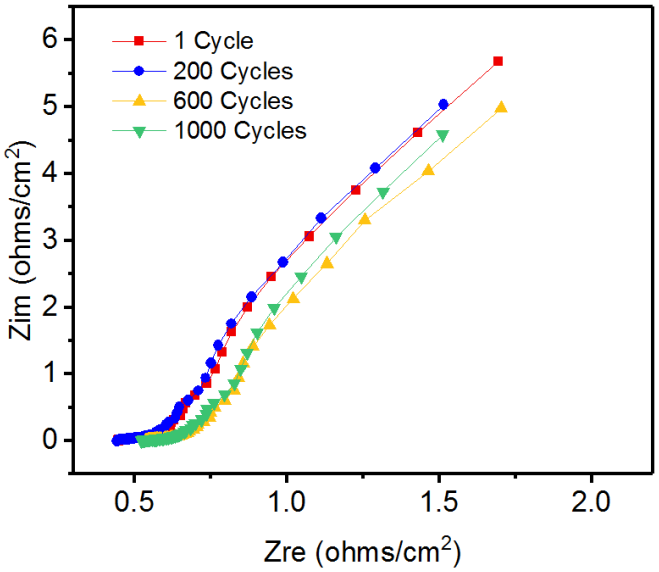

Figure 3.40: Nyquist plots of $Ni(OH)_2$-CTAB electrode at 0 V *vs.* Hg/Hg_2Cl_2 at various cycles.

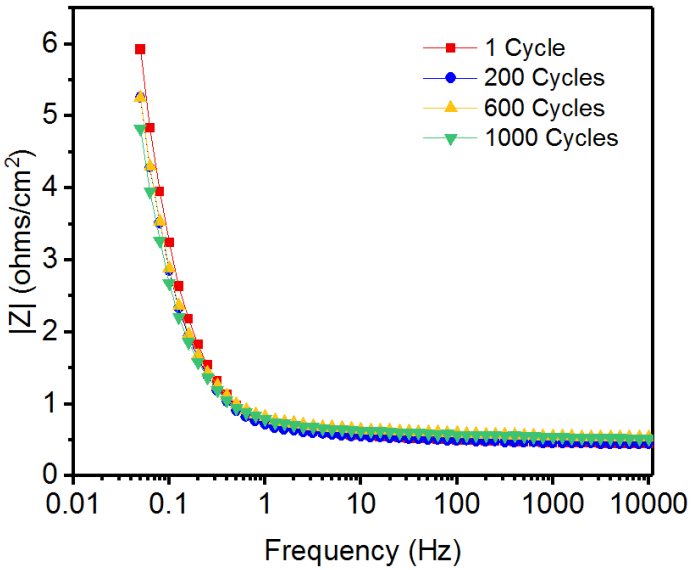

Figure 3.41: Impedance as a function of frequency plot of $Ni(OH)_2$-CTAB electrode at 0 V *vs.* Hg/Hg_2Cl_2 at various cycles.

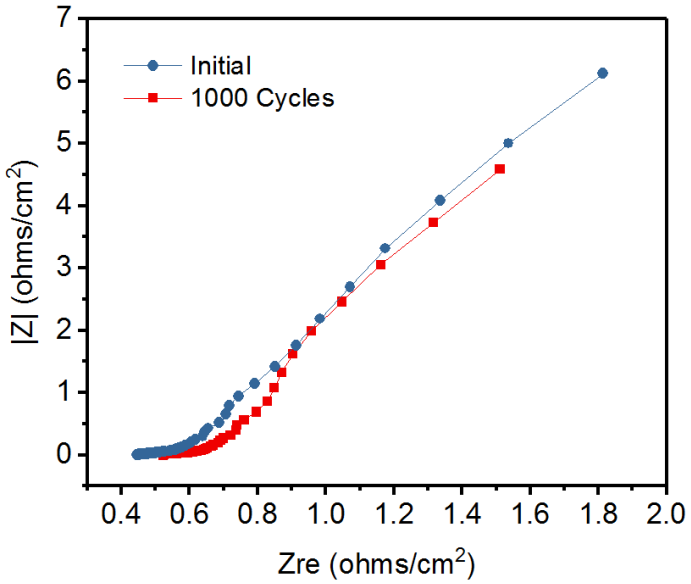

Figure 3.42: Nyquist plots of $Ni(OH)_2$-CTAB electrode at 0 V *vs.* Hg/Hg_2Cl_2 for the initial cycle and the 1000th cycle.

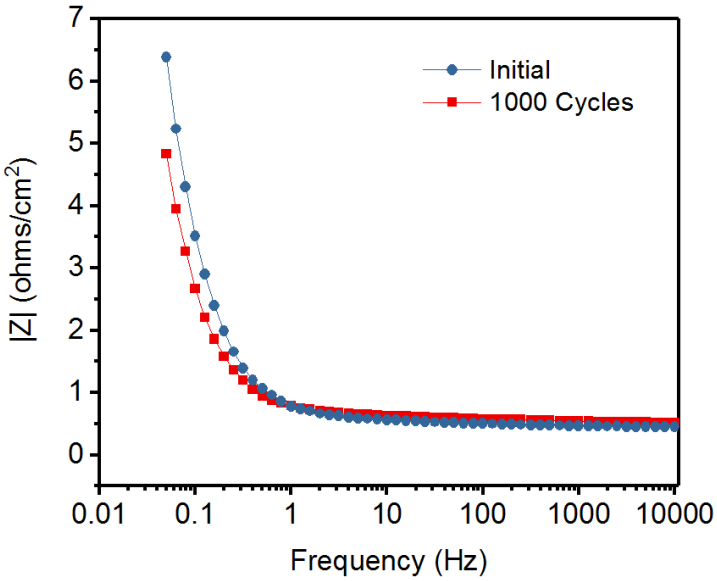

Figure 3.43: Impedance as a function of frequency plot of $Ni(OH)_2$-CTAB electrode at 0 V *vs.* Hg/Hg_2Cl_2 for the initial cycle and the 1000th cycle.

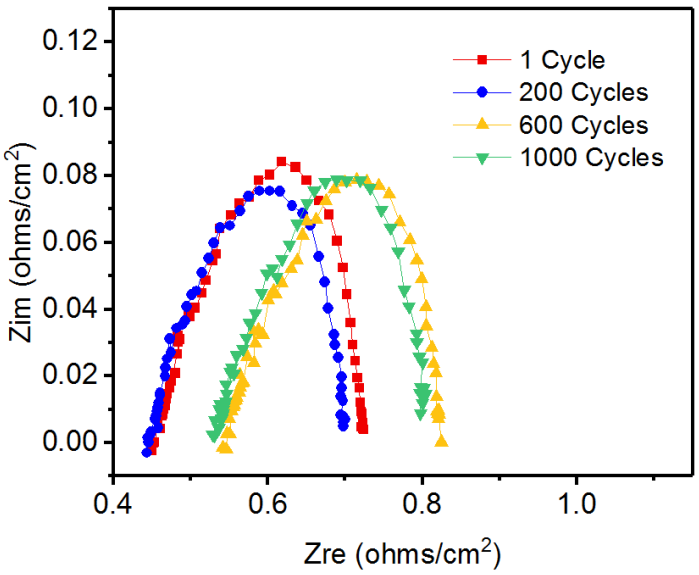

Figure 3.44: Nyquist plots of $Ni(OH)_2$-CTAB electrode at 0.55 V *vs.* Hg/Hg_2Cl_2 at various cycles.

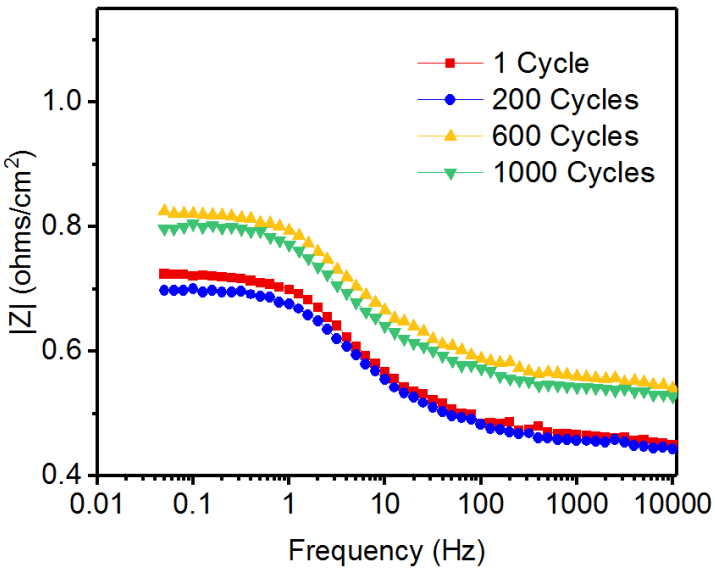

Figure 3.45: Impedance as a function of frequency plot of $Ni(OH)_2$-CTAB electrode at 0.55 V *vs.* Hg/Hg_2Cl_2 at various cycles.

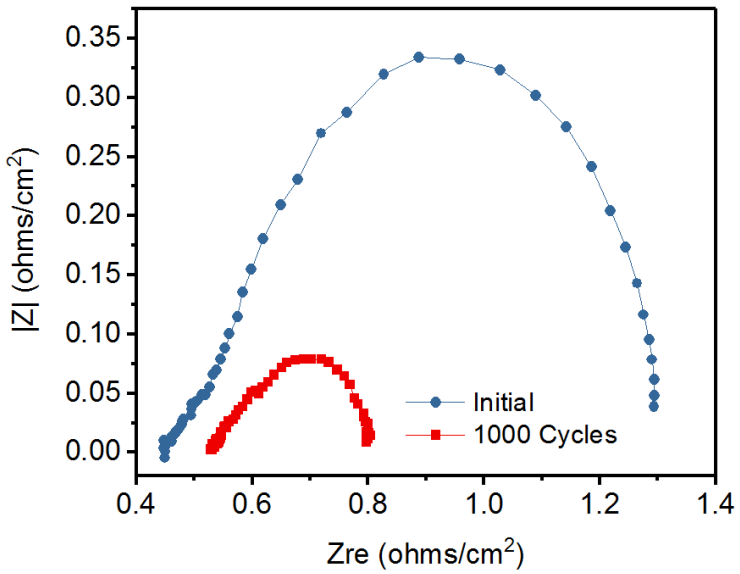

Figure 3.46: Nyquist plots of $Ni(OH)_2$-CTAB electrode at 0.5 V *vs.* Hg/Hg_2Cl_2 for the initial cycle and the 1000th cycle.

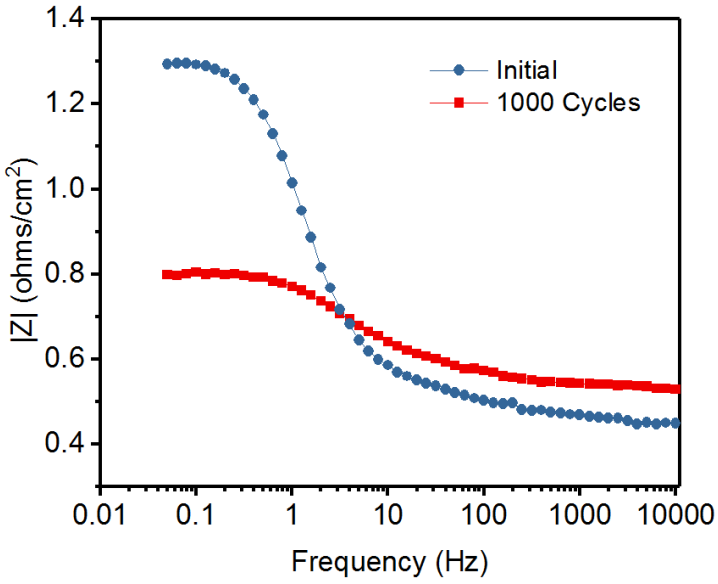

Figure 3.47: Impedance as a function of frequency plot of $Ni(OH)_2$-CTAB electrode at 0.5 V *vs.* Hg/Hg_2Cl_2 at for the initial cycle and the 1000th cycle.

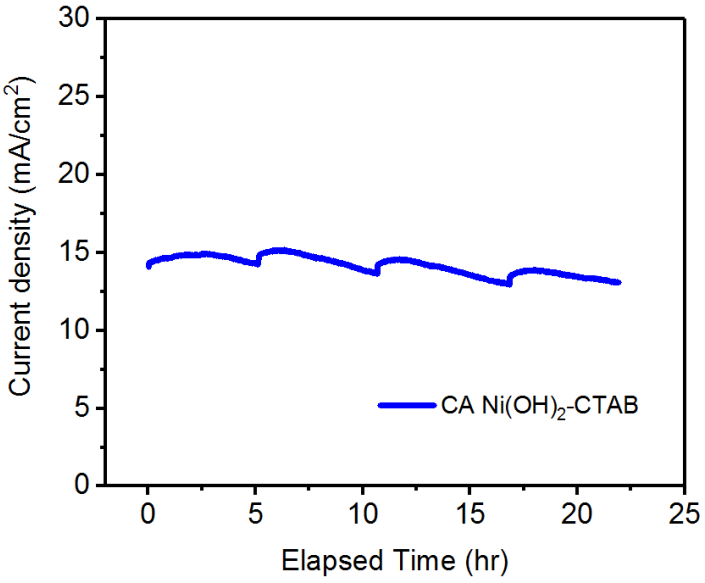

Figure 3.48: Time-dependent current density curve for the synthesized $Ni(OH)_2$-CTAB electrode.

3.3.2 Electrocatalyst for Hydrogen Evolution Reaction

In 1M of KOH, the electrocatalytic performance of all the electrodes was investigated for a hydrogen evolution reaction using a three-electrode system. **Figure 3.49** shows the HER polarization curves of $Ni(OH)_2$-PVP, $Ni(OH)_2$-CTAB, NiO-PVP, NiO-CTAB, NiS_2-PVP, and NiS_2-CTAB grown on nickel foam. The obtained electrodes required overpotentials of 177, 189, 199, 218, 200, and 182 mV to reach 10 mA/cm^2, respectively. The $Ni(OH)_2$-PVP shows the best HER activity compared with other electrodes. The Tafel slope was also determined via LSV curves. The Tafel slope for the $Ni(OH)_2$-PVP electrode is 107 mV per decade, being lower than other electrodes of $Ni(OH)_2$-CTAB 123 mV/dec, NiO-PVP 140 mV/dec, NiO-CTAB 143 mV/dec, NiS_2-PVP 149 mV/dec, and NiS_2-CTAB 155 mV/dec as shown in **Figure 3.50**. Besides, the $Ni(OH)_2$-PVP electrode exhibited a lower charge transfer résistance compared with other electrodes.

Figures 3.51-3.54 illustrate the Nyquist plots and the impedance as a function of frequency for the electrodes at a potential of 0 and -1.25 (V *vs.* Hg/Hg_2Cl_2). The $Ni(OH)_2$-PVP showed the lowest resistance of 4 Ω while resistances of 6.5, 6.5, 12, 9, and 8 Ω were exhibited for $Ni(OH)_2$-CTAB, NiO-PVP, NiO-CTAB, NiS_2-PVP, and NiS_2-CTAB, respectively, at -1.25 V. At a low-frequency region, the $Ni(OH)_2$-PVP shows a semicircle shape, which is associated with charge transfer resistance. As the value of charge transfer resistance decreases, the electrochemical reaction rate increases, leading to faster charge transfer transport and better performance. However, Sivanantham, *et. al*., have successfully synthesized $NiCo_2S_4$ nanowire arrays supported on Ni foam ($NiCo_2S_4$ NW/NF) using a pressurized hydrothermal method. They observed that the ($NiCo_2S_4$ NW/NF) electrode showed an overpotential of 210 mV to generate 10 mA/cm^2 current density for HER in 1M of KOH electrolyte solution [37]. Also, they have studied other electrodes, such as Ni_3S_2/NF and $NiCo_2O_4$/NF, and it was observed that both electrodes showed the same overpotential of 310 mV at a current density of 10 mA/cm^2 [37]. YU, *et. al*., have synthesized α-$Ni(OH)_2$ on the surface of platinum; the overpotential was reported to be 278 mV in 0.1M KOH at a current densiyty of 10 mA/cm^2 [38]. Furthermore, Ai, *et. al.*, who reported "a composite architecture that consists of onion-like ultrathin graphene shells encapsulating uniform metallic nickel nanoparticles (Ni@graphene) derived by a straightforward thermal treatment of a Ni-based metal−organic framework in an inert atmosphere," observed an overpotential of 240 mV at 10 mA/cm^2 current density [35]. The overpotentials of the electrodes at a current density of 10 mA/cm^2 and the corresponding Tafel slopes are listed in **Tables 7 and 8**.

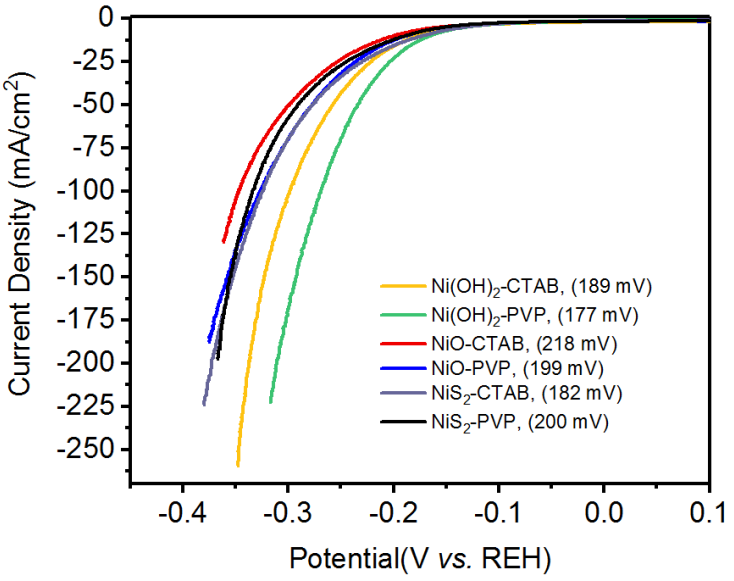

Figure 3.49: LSV polarization curves for all the synthesized electrodes.

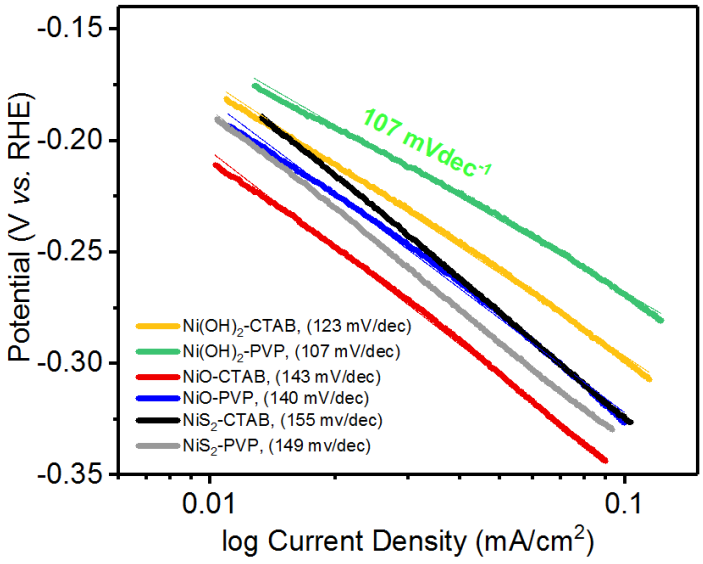

Figure 3.50: Represent the corresponding Tafel slopes for all the synthesized electrodes.

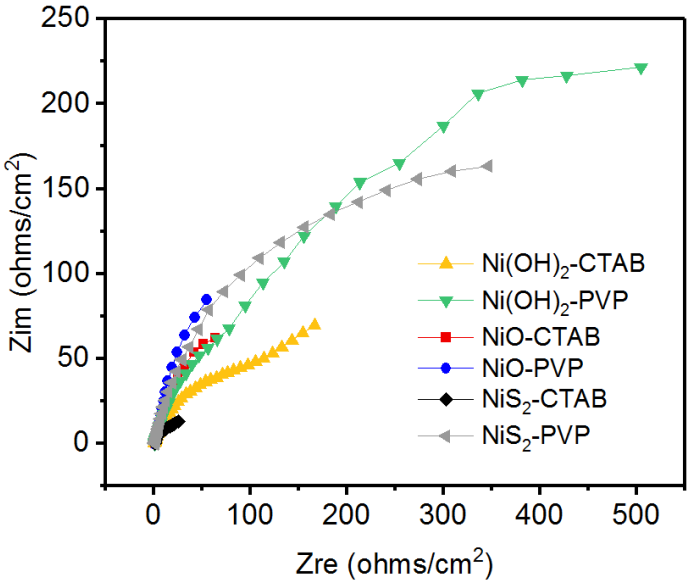

Figure 3.51: Nyquist plots of all the catalyst electrodes at 0 V *vs.* Hg/Hg$_2$Cl$_2$.

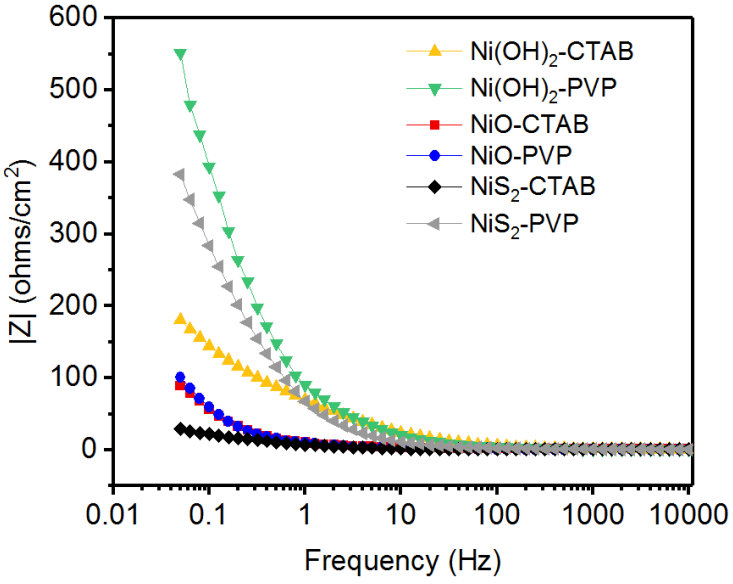

Figure 3.52: Impedance as a function of frequency for all the catalyst electrodes at 0 V *vs.* Hg/Hg$_2$Cl$_2$.

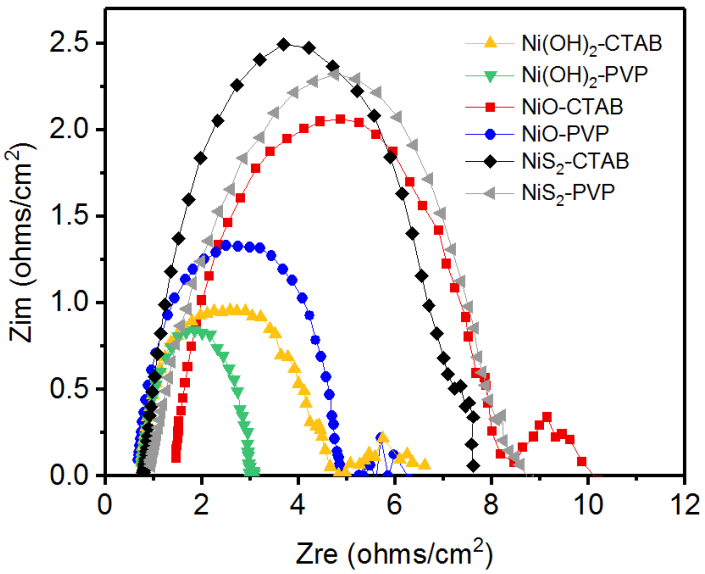

Figure 3.53: Nyquist plots of all the catalyst electrodes at -1.25V *vs.* Hg/Hg_2Cl_2.

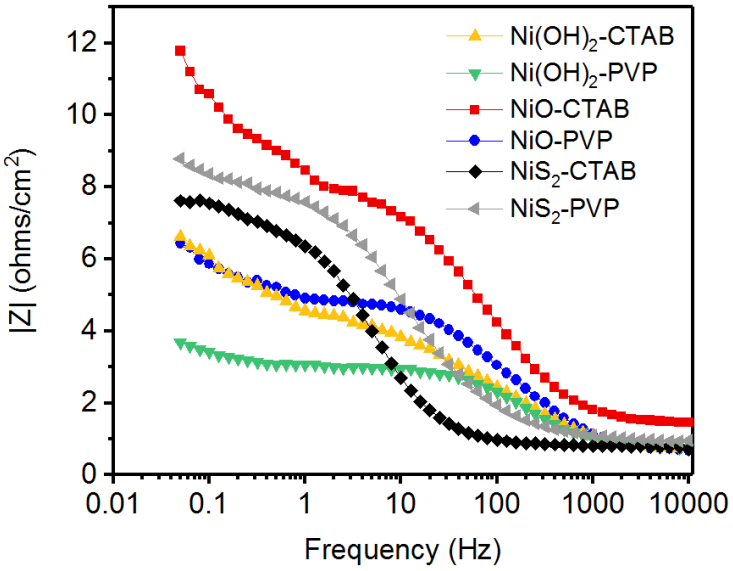

Figure 3.54: Impedance as a function of frequency for all the catalyst electrodes at -1.25 V *vs.* Hg/Hg_2Cl_2.

Table 7: The HER overpotentials of all the synthesized electrodes at a current density of 10 mA/cm^2 and the corresponding Tafel slopes.

Electrode	*Overpotential (mV)*	*Tafel Slope (mV/dec)*
$Ni(OH)_2$-PVP	177	109
$Ni(OH)_2$-CTAB	189	123
NiO-PVP	199	138
NiO-CTAB	218	140
NiS_2-PVP	200	149
NiS_2-CTAB	182	155

Table 8: Results of HER electrodes at 10 mA/cm^2 of other reports.

Electrode	*Overpotential (mV)*
α-$Ni(OH)_2$	278
Ni_3S_2/NF	310
$NiCo_2S_4$ NW/NF	210
$NiCo_2O_4$/NF	310

CHAPTER IV

CONCLUSION

In summary, a facile hydrothermal technique and a binder-free approach were used to synthesize nanostructured $Ni(OH)_2$, NiO, and NiS_2 in the presence of cetyltrimethylammonium bromide and polyvinylpyrrolidone on nickel foams. The synthesized nanostructured materials ($Ni(OH)_2$-CTAB, $Ni(OH)_2$-PVP, NiO-CTAB, NiO-PVP, NiS_2-CTAB, and NiS_2-PVP) were used for both supercapacitor applications and as catalysts for water splitting. The structures, morphologies, and electrochemical performances of the synthesized nickel compounds were analyzed and characterized using a variety of techniques. The structural characterizations were analyzed via X-ray diffraction, and scanning electron microscopy. The morphological structure and the size of the samples were observed to depend on the growth condition and presence of CTAB and PVP.

The electrochemical performances of the samples toward supercapacitor and catalyst applications were performed in a standard three-electrode system using potassium hydroxide as an electrolyte, a Pt wire as a counter electrode, a saturated calomel electrode as a reference electrode, and the synthesized electrodes as a working electrode. The areal capacitances were observed to be 50, 67, 529, 859, 1,211, and 2,633 mF/cm^2 for NiO-PVP, NiO-CTAB, $Ni(OH)_2$-PVP, $Ni(OH)_2$-CTAB, NiS_2-PVP, and NiS_2-CTAB, respectively.

Additionally, the electrocatalytic performances toward oxygen evolution and hydrogen evolution reaction were investigated. The NiS_2-CTAB electrode showed the lowest OER overpotential of 298 mV at 10 mA/cm^2 and a Tafel slope of 111 mV/dec. The lowest HER overpotential of 177 mV at 10 mA/cm^2 was observed for the $Ni(OH)_2$-PVP electrode.

The electrochemical performance of the synthesized nanostructured materials revealed that their properties depend on the presence of CTAB and PVP during synthesis. Our results suggest that nickel based nanostructured materials could be used as bi-functional materials for energy storage and generation.

REFERENCES

1. Asif, M. & Muneer, T. Energy supply, its demand and security issues for developed and emerging economies. *Renewable and Sustainable Energy Reviews* **11,** 1388–1413 (2007).
2. Jacobson, M. Z. & Delucchi, M. A. Providing all global energy with wind, water, and solar power, Part I: Technologies, energy resources, quantities, and areas of infrastructure, and materials. *Energy Policy* **39,** 1154–1169 (2011).
3. Kalyanasundaram, K. & Graetzel, M. Artificial photosynthesis: biomimetic approaches to solar energy conversion and storage. *Currrent Opinion in Biotechnology* **21,** 298–310 (2010).
4. Goswami, D. Y. A review of engineering developments of aqueous phase solar photocatalytic detoxification and disinfection processes. *Journal of Solar Energy Engineering* **119,** 101-107 (1997).
5. Kanchev, H., Lu, D., Colas, F., Lazarov, V. & Francois, B. Energy management and operational planning of a microgrid with a pv-based active generator for smart grid applications. *IEEE Transactions on Industrial Electronics* **58,** 4583–4592 (2011).
6. Ranaweera, C. K. *et al.* Flower-shaped cobalt oxide nano-structures as an efficient, flexible and stable electrocatalyst for the oxygen evolution reaction. *Materials Chemistry Frontiers* **1,** 1580–1584 (2017).
7. Ibrahim, H., Ilinca, A. & Perron, J. Energy storage systems—characteristics and comparisons. *Renewable and Sustainable Energy Reviews* **12,** 1221–1250 (2008).
8. Sarangapani, S., Tilak, B. V. & Chen, C. -P. Materials for electrochemical capacitors. *Journals of Electrochemical Society* **143,** 3791 (1996).

9. Winter, M. & Brodd*, R. J. What are batteries, fuel cells, and supercapacitors?. Chemical Reviews **104,** 4245-4270 (2004).

10. Carrette, L., Friedrich, K. A. & Stimming, U. Fuel cells - fundamentals and pplications. *Fuel Cells* **1,** 5–39 (2001).

11. Schiffer, M. B. Studying technological differentiation: The case of 18th-century electrical technology. *American Anthropologist* **104,** 1148–1161 (2002).

12. Yoshida, T., Kitoh, K., Mori, T., Katsukawa, H. & Yamaki, J. Influence of electrode active materials on safety performance of large and high-power Li-ion batteries for hybrid electric vehicles. *Electrochemical and Solid-State Letters* **9,** A458-A462 (2006).

13. Kötz, R. & Carlen, M. Principles and applications of electrochemical capacitors. *Electrochimica Acta* **45,** 2483–2498 (2000).

14. Kou, L. *et al.* Coaxial wet-spun yarn supercapacitors for high-energy density and safe wearable electronics. *Nature Communications* **5,** 3754 (2014).

15. Wang, G., Zhang, L. & Zhang, J. A review of electrode materials for electrochemical supercapacitors. *Cheminform Society Review* **41,** 797–828 (2012).

16. Wang, Y., Song, Y. & Xia, Y. Electrochemical capacitors: mechanism, materials, systems, characterization, and applications. *Chemical Society Reviews* **45,** 5925–5950 (2016).

17. Kim, I.-H., Kim, J.-H. & Kim, K.-B. Electrochemical characterization of electrochemically prepared ruthenium oxide/carbon nanotube electrode for supercapacitor application. *Electrochemical and Solid-State Letters* **8,** A369-A372 (2005).

18. Qi, Z., Huang, S., Younis, A., Chu, D. & Li, S. Nanostructured metal oxide-based electrode in *supercapacitor applications. Supercapacitor Design and Applications* **7,** 411-456 (2016).

19. Wang, Y. *et al.* Mesoporous transition metal oxides for supercapacitors. *Nanomaterials* **5,** 1667–1689 (2015).

20. Hu, W. *et al.* $CoNi_2S_4$ Nanosheet arrays supported on nickel foams with ultrahigh capacitance for aqueous asymmetric supercapacitor applications. *ACS Applied Materials & Interfaces* **6,** 19318–19326 (2014).

21. Bandal, H. A., Jadhav, A. R., Tamboli, A. H. & Kim, H. Bimetallic iron cobalt oxide self-supported on Ni-foam: an efficient bifunctional electrocatalyst for oxygen and hydrogen evolution reaction. *Electrochimica Acta* **249,** 253–262 (2017).

22. Wang, R., Wu, K. & Wu, C. Highly sensitive electrochemical detection of bisphenol A based on the cooperative enhancement effect of the graphene–$Ni(OH)_2$ hybrid and hexadecyltrimethylammonium bromide. *Analytical Methods* **7,** 9261–9267 (2015).

23. Ma, Z. *et al.* Novel flower-like nickel sulfide as an efficient electrocatalyst for non-aqueous lithium-air batteries. *Scientific Reports.* **5,** 18199 (2016).

24. Yan, H. *et al.* Solution growth of NiO nanosheets supported on Ni foam as high-performance electrodes for supercapacitors. *Nanoscale Research Letters* **9,** 1-7 (2014).

25. Jiang, S. *et al.* High-performance binder-free supercapacitor electrode by direct growth of cobalt-manganese composite oxide nansostructures on nickel foam. *Nanoscale Research Letters* **9,** 1-8 (2014).

26. Zhang, J. *et al.* Facile synthesis of a nickel sulfide (NiS) hierarchical flower for the

electrochemical oxidation of H_2O_2 and the methanol oxidation reaction (MOR). *Journal of Electrochemical Society* **164,** B92–B96 (2017).

27. Gupta, R. K., Candler, J., Palchoudhury, S., Ramasamy, K. & Gupta, B. K. Flexible and high performance supercapacitors based on $NiCo_2O_4$ for wide temperature range applications. *Scientific Reports* **5,** 15265 (2015).

28. Jiang, H., Zhao, T., Li, C. & Ma, J. Hierarchical self-assembly of ultrathin nickel hydroxide nanoflakes for high-performance supercapacitors. *Journal of Materials Chemistry* **21,** 3818-3823 (2011).

29. Liu, B. *et al.* New energy storage option: toward $ZnCo_2O_4$ nanorods/nickel foam architectures for high-performance supercapacitors. *ACS Applied Materials & Interfaces* **5,** 10011–10017 (2013).

30. Cai, W. *et al.* Transition metal sulfides grown on graphene fibers for wearable asymmetric supercapacitors with high volumetric capacitance and high energy density. *Scientific Reports* **6,** 26890 (2016).

31. Liu, X., You, B., Yu, X.-Y., Chipman, J. & Sun, Y. Electrochemical oxidation to construct a nickel sulfide/oxide heterostructure with improvement of capacitance. *Journal of Materials Chemistry. A* **4,** 11611–11615 (2016).

32. Qiu, Z., Ma, Y., Edström, K., Niklasson, G. A. & Edvinsson, T. Controlled crystal growth orientation and surface charge effects in self-assembled nickel oxide nanoflakes and their activity for the oxygen evolution reaction. *International Journal of Hydrogen Energy* **42,** 28397–28407 (2017).

33. Zhou, Y. & Zeng, H. C. Metal–hydroxide and gold–nanocluster interfaces: enhancing catalyst activity and stability for oxygen evolution reaction. The *Journal*

of Physical Chemistry C **120,** 29348–29357 (2016).

34. Zhou, X., Xia, Z., Zhang, Z., Ma, Y. & Qu, Y. One-step synthesis of multi-walled carbon nanotubes/ultra-thin $Ni(OH)_2$ nanoplate composite as efficient catalysts for water oxidation. *Journal of Material Chemistry A* **2,** 11799–11806 (2014).
35. Ai, L., Tian, T. & Jiang, J. Ultrathin graphene layers encapsulating nickel nanoparticles derived metal–organic frameworks for highly efficient electrocatalytic hydrogen and oxygen evolution reactions. *ACS Sustainable Chemistry & Engineering* **5,** 4771–4777 (2017).
36. Xiao, X. *et al.* Engineering NiS/Ni_2 P Heterostructures for efficient electrocatalytic water splitting. *ACS Applied Materials & Interfaces* **10,** 4689–4696 (2018).
37. Sivanantham, A., Ganesan, P. & Shanmugam, S. Bifunctional electrocatalysts: hierarchical $NiCo_2S_4$ nanowire arrays supported on Ni foam: an efficient and durable bifunctional electrocatalyst for oxygen and hydrogen evolution reactions. *Advanced Functional Materials* **26,** 4660–4660 (2016).
38. Yu, X. *et al.* Hydrogen evolution reaction in alkaline media: alpha- or beta-nickel hydroxide on the surface of platinum?. *ACS Energy Letters* **3,** 237–244 (2018).